

1 Shear velocity inversion guided by resistivity structure from the PI-LAB
2 Experiment for integrated estimates of partial melt in the mantle

3
4 Nicholas Harmon¹, Shunguo Wang², Catherine A. Rychert¹, Steven Constable³, J Michael
5 Kendall⁴

6
7 ¹ University of Southampton, Ocean and Earth Science, Southampton, UK

8 ² Norwegian University of Science and Technology, Department of Electronic Systems,
9 Trondheim, Norway

10 ³ University of California San Diego, Scripps Institution of Oceanography, San Diego, USA

11 ⁴ Oxford University, Department of Earth Science, Oxford, UK

12 **Abstract**

13 The lithosphere-asthenosphere system is fundamental to our understanding of mantle
14 convection and plate tectonics. The different sensitivities of seismic and electromagnetic
15 methods can be used together to better constrain the properties of the system. Here we re-
16 examine the shear velocity model from Rayleigh waves in light of the magnetotelluric based
17 resistivity models from the PI-LAB experiment near the equatorial Mid-Atlantic Ridge, with
18 the goal of generating a structurally consistent velocity and resistivity model for the region.
19 Cross-plots of the models suggest a linear or near-linear trend that is also in agreement with
20 petrophysical predictions. We generate a new shear velocity model from the resistivity
21 models based on petrophysical relationships. The new velocity model fits the phase velocity
22 data, and the correlation coefficient between the shear velocity and resistivity models is
23 increased. Much of the model can be predicted by expectations for a thermal half-space
24 cooling model, although some regions require a combination of higher temperatures,
25 volatiles, or partial melt. We use the petrophysical predictions to estimate the melt fraction,
26 melt volatile content, and temperature structure of the asthenospheric anomalies. We find
27 up to 4% melt, with the lowest resistivities and shear velocities explained by up to 20%
28 water or 20% CO₂ in the melt or ~1% nearly pure sulfide melt, depending on the set of
29 assumptions used. Melt is required in punctuated anomalies over broad depth ranges, and
30 also in channels at the base of the lithosphere. Melt in the asthenosphere is dynamic, yet
31 persistent on geologic time scales.

32
33 **Introduction**

34 Plate tectonic theory is predicated on the idea of a rigid lithosphere that overrides a weaker
35 underlying asthenosphere (McKenzie & Parker, 1967), but the nature of the lithosphere-
36 asthenosphere system remains the subject of vigorous debate. The oceanic lithosphere
37 comprises the majority of the surface of the Earth and has the simplest evolution and
38 history. It is classically thought to be thermally defined as a boundary layer in a simple
39 thermal model (Parker & Oldenburg, 1973). In this model, increasing temperature with
40 depth causes mantle rocks to weaken, creating the asthenosphere (e.g., Goetze et al., 1978).
41 However, a host of observations, including sharp seismic velocity discontinuities (Gaherty et
42 al., 1996; Kawakatsu et al., 2009; Rychert et al., 2020; Rychert et al., 2018; Rychert &
43 Shearer, 2011; Schmerr, 2012; Tan & Helmberger, 2007; Tharimena et al., 2017), low

44 velocity zones (Forsyth et al., 1998; Harmon et al., 2020), and low resistivity zones (Baba et
45 al., 2006; Johansen et al., 2019; Key et al., 2013; Naif et al., 2013; Wang et al., 2020) in the
46 asthenosphere, suggest that in addition to temperature other factors are likely required to
47 explain the observations. Many potential explanations of these observations have been
48 proposed including an increased effect of hydration (Karato, 2012), the presence of partial
49 melt (Anderson & Sammis, 1970; Kawakatsu et al., 2009), and/or the enhanced effects at
50 near sub-solidus conditions on seismic waves (Yamauchi & Takei, 2016). The debate centers
51 around which of these explanations might be in operation and how widely they apply.

52
53 Partial melt is an attractive possibility given that it provides an explanation for a wide range
54 of observations with different sensitivities (Rychert et al., 2020). Partial melt likely to exist in
55 the asthenosphere, in particular near mid-ocean ridges and volcanic arcs where the volcanic
56 systems must be fed by mantle melting (Anderson & Sammis, 1970). However, further away
57 from volcanic plate boundaries its presence is debated (Kawakatsu et al., 2009; Priestley &
58 McKenzie, 2006; Rychert et al., 2005). The amount of melt and its location is vital to our
59 understanding of how the lithosphere-asthenosphere works, as the presence of partial melt
60 is predicted to reduce the viscosity of the asthenosphere (Hirth & Kohlstedt, 1995; Jackson
61 et al., 2006) and could also facilitate plate tectonics (Rychert et al., 2005; Rychert et al.,
62 2007). However, different geophysical techniques with different sensitivities and resolutions
63 have imaged anomalies that have been interpreted as melt in many forms (Rychert et al.,
64 2020). For instance beneath mid-ocean ridges, seismic surface wave studies have
65 interpreted a broad, hundreds of kilometers wide, melt triangle beneath the ultrafast
66 spreading East Pacific Rise at 17 °S (Dunn & Forsyth, 2003; Forsyth et al., 1998) and the
67 intermediate spreading Juan De Fuca Ridge (Bell et al., 2016; Gao, 2016), while other studies
68 have imaged smaller scale and discrete melt zones beneath the slow spreading equatorial
69 Mid-Atlantic Ridges on the order of 100-200 km wide (Harmon et al., 2020). The
70 magnetotelluric (MT) method has typically imaged smaller and more discrete low resistivity
71 zones interpreted as focused melt regions beneath the fast spreading East Pacific Rise at 9
72 °N and the ultra-slow spreading Mohns Ridge (Johansen et al., 2019; Key et al., 2013) that
73 are typically < 100 km wide, although a broader region >200 km was inferred beneath the
74 East Pacific Rise at 17 °S (Evans et al., 1999). Further off-axis, layered and/or pervasive melt
75 in the asthenosphere has been inferred based on the imaging of discontinuities by scattered
76 waves that require sharp drops in seismic velocity with depth (Kawakatsu et al., 2009;
77 Rychert & Shearer, 2011; Rychert & Shearer, 2009; Tharimena et al., 2017). Active source
78 seismic studies also find strong reflectors near the expected base of the tectonic plate, that
79 have been interpreted as channelized melt (Mehouachi & Singh, 2018; Stern et al., 2015).
80 Similar channelized structures have also been interpreted from thin low resistivity zones at
81 60-80 km depth (Naif et al., 2013; Wang et al., 2020). Whether or not differences among the
82 inferred shape and location of melt are an artefact of resolution and sensitivities of the
83 individual methodologies or representative of real Earth structure has remained unclear.

84
85 The complementary resolution and sensitivities of MT and seismic imaging techniques offer
86 a promising means of probing Earth's physical properties to examine the thermal structure
87 and the presence of partial melt. The Earth's mantle is primarily composed of olivine and
88 pyroxene, and the conductivity of these minerals has a strong temperature dependence
89 (Gardés et al., 2014; Naif et al., 2021), enhanced by the presence of conducting fluids such
90 as partial melt (Naif et al., 2021; Ni et al., 2011) and the presence of water and other

91 crystallographic defects in the olivine mineral lattice (Gardés et al., 2014; Naif et al., 2021).
92 Water and other volatiles such as CO₂ are also thought to significantly increase the
93 conductivity of the fluid and therefore the overall conductivity of the mantle if present (Ni
94 et al., 2011; Sifre et al., 2014). On the other hand, seismic velocities are dependent on
95 temperature and pressure (e.g., Stixrude & Lithgow-Bertelloni, 2005), followed by the
96 presence of partial melt (Clark & Lesher, 2017; Hammond & Humphreys, 2000), particularly
97 for shear velocity, and are relatively insensitive to the presence of water as a
98 crystallographic defect (Abers et al., 2014) or as a component of the partial melt. These
99 differences mean that the two methods together have the potential to better constrain the
100 thermal properties of the mantle, the presence and amount of partial melt, and the amount
101 of hydration in the melt.

102 There have been two main approaches to cooperative or simultaneous joint inversion of
103 electromagnetic and seismic data: 1) inversion based on underlying petrophysical or
104 empirical relationships between velocity and conductivity (Abubakar et al., 2012; Jegen et
105 al., 2009; Sun & Li, 2016; Takougang et al., 2015) and 2) inversion based on model gradient
106 approaches, e.g., forcing model changes in velocity and resistivity either in the same sense,
107 the opposite sense, or with no change in one of the models (Bennington et al., 2015;
108 Gallardo & Meju, 2004; Haber & Oldenburg, 1997; Moorkamp et al., 2011; Zhang et al.,
109 2020). The petrophysical or empirical approach requires either accurate models of the
110 physical properties of the rocks (Gardés et al., 2014), an (ideally) relatively simple system
111 that can be captured with simple linear or polynomial fits to data (Jegen et al., 2009), or a
112 guided fuzzy c-means clustering operator (Sun & Li, 2016), which is more likely the case in
113 locations with limited compositional and thermal variation. However, the success of this
114 approach depends strongly on the accuracy of the prior information and laboratory
115 measurements, which is specific to the area of interest since the relationship between
116 velocity and conductivity is not universal. The model gradient approach, such as cross
117 gradient (Gallardo & Meju, 2004) and normalized cross gradient (Zhang et al., 2020), on the
118 other hand, presumes that the gradient of resistivity structures is positively or negatively
119 correlated with the gradient of velocity structures. The minimization of model gradient or
120 cross-gradient can also be satisfied automatically where zero gradient is required by one or
121 both datasets. In contrast with the petrophysical approach, the gradient method is more
122 generic. The cross-gradient approach is probably more useful for detecting regions where
123 the physical and chemical properties of the Earth result in seismic and resistivity anomalies
124 that would not necessarily align. For instance, the presence of small amounts of certain
125 minerals such as magnetite in serpentine (Stesky & Brace, 1973) or graphite (Frost et al.,
126 1989) and other highly conductive minerals would generate a strong resistivity anomaly, but
127 may not be volumetrically significant enough to have a strong seismic signature. Choosing
128 between these two approaches or other approaches using Monte Carlo inversions
129 (Moorkamp et al., 2010) is dependent on the details of the particular datasets and the
130 structure involved. Combining the two approaches is possible, and exhibits enhanced
131 performance for structural similarity in the joint inversion (Colombo & Rovetta, 2018; Guo
132 et al., 2020).

134
135 The I-LAB (Imaging the Lithosphere-Asthenosphere Boundary) experiments including: 1)
136 Passive Imaging of the Lithosphere Asthenosphere Boundary (PI-LAB) experiment, 2)
137 Experiment to Unearth the Rheological Lithosphere-Asthenosphere Boundary (EURO-LAB),

138 and 3) the Central Atlantic Lithosphere-Asthenosphere Boundary (CA-LAB) experiment
139 presented a unique opportunity for interpretation of MT and seismic data in order to
140 understand the oceanic lithosphere-asthenosphere system at the equatorial Mid-Atlantic
141 Ridge. We deployed 39 ocean bottom seismometers (OBS) and 39 ocean bottom
142 magnetotelluric (OBMT) instruments on 0-80 Myr seafloor across the long offset Chain and
143 Romanche fracture zones (Agius et al., 2018; Harmon et al., 2018), allowing us to sample a
144 wide seafloor age range in one experiment. The OBS and OBMT were co-located (within 1-2
145 km), in three lines perpendicular to the ridge (Fig. 1). The experiment was designed to image
146 the uppermost mantle beneath the ridge system and examine the evolution of the oceanic
147 lithosphere-asthenosphere system and the nature of the lithosphere-asthenosphere
148 boundary.

149
150 Here we focus on two results for developing a structurally consistent model of the oceanic
151 lithosphere-asthenosphere system, the three-dimensional (3-D) shear-wave velocity model
152 from Rayleigh wave tomography and the two-dimensional (2-D) MT inversions from the two
153 southernmost lines (Fig. 1, 2). The shear velocity model images a high velocity lithosphere,
154 and several punctuated low velocity zones (<4.2 km/s) in the asthenosphere, that were
155 interpreted as melt (Harmon et al., 2020). Near the ridge axis, asthenospheric low velocity
156 zones are attributed to sub-ridge upwelling (Anomalies A and E in line I and line II,
157 respectively in Fig. 2), while further off-axis the low velocity anomalies are attributed to
158 melting due to upwelling caused by small scale convection (Anomalies B, C, and F in Fig. 2)
159 (Harmon et al., 2020; Wang et al., 2020). The MT result images similar structures to the
160 surface wave model, e.g., a high resistivity lithospheric lid ($\log_{10}(\rho) > 2$) and several low
161 resistivity anomalies ($\log_{10}(\rho) < 1$) in the asthenosphere (anomalies A, B, C, D, E, and F in Fig.
162 2) (Wang et al., 2020). In Line I there is good agreement with the depth (50-80 km) and
163 lateral extent (~100-200 km) of the low resistivity anomaly and low seismic velocities
164 (Anomalies B and C) as well as evidence for a high resistivity, high velocity lithospheric drip
165 (anomaly D) that extended from 50 to 150 km depth. However, in line II (Fig. 2b and 2d) the
166 agreement in terms of the shapes of the anomalies is less remarkable, specifically anomaly
167 F, where the conductive anomalies suggest a channel structure < 20 km thick extending
168 from the ridge to 30 Myr seafloor, while the surface wave anomaly resembles a simple oval
169 ~200 km wide from 50-80 km depth. In addition, anomaly E is deeper in the resistivity
170 model, >100 km depth, than in the shear velocity model, where it extends from 50 to 100
171 km depth. While in line I, anomaly A is shallower at ~30 km depth and smaller, <50 km wide,
172 in the resistivity model than in the shear velocity model, where it is located at 50-80 km
173 depth and 150 km wide. In other words, while there is some similarity in the lateral
174 locations of the anomalies, the exact depth and morphologies are somewhat different.

175
176 Subsequent studies support the existence of these anomalies and suggest that apparent
177 discrepancies may be artefacts of resolution. For example, S-to-P receiver functions support
178 the existence of the anomalies (Rychert et al., 2021). The receiver functions image
179 discontinuities associated with sharp velocity decreases with depth above the locations of
180 the low shear velocity anomalies E, C, and F in the asthenosphere and also the locations
181 where the low resistivity anomalies gradually decrease with depth in the asthenosphere
182 (near anomaly E and directly beneath F) (Rychert et al., 2021). In addition, a short period
183 Rayleigh wave tomography study, which had better resolution in the upper 60 km than
184 Harmon et al. (2020), imaged a shallower anomaly for anomaly A beneath line I, more

185 consistent with the resistivity model (Saikia et al., 2021). The differences between the
186 surface wave models suggest that there are several possibilities for shear-wave velocity
187 models that will fit the Rayleigh wave data. Some of these shear velocity models could also
188 be consistent with the anomaly structure of the resistivity models as well, noting that the
189 MT method is preferentially sensitive to conductors, such as the anomalies C and F at the
190 LAB depths. Therefore, the primary motivation of this study is to find a satisfactory shear
191 velocity model that is also consistent with structural information from the resistivity models.
192

193 Here we jointly consider the Rayleigh wave phase velocities and the MT data to evaluate
194 differences and similarities between the seismic and MT anomaly structures, in particular to
195 determine an Earth structure that can satisfy both datasets within data errors. We compare
196 the models one-to-one to develop an empirical relationship between the two. Since the
197 observed relationship is very similar to laboratory-based predictions for shear velocity and
198 resistivity, we proceed using the laboratory-based relationship to translate the MT resistivity
199 to shear-wave velocity. We use the MT-derived shear velocity model as the new starting
200 model for the surface wave tomography inversion. This approach assumes that the
201 structure within the resistivity model is closer to the true earth structure, which may be the
202 case, for example, if a thin channel structure exists, which surface waves would not be able
203 to resolve without prior knowledge (e.g., Rychert et al., 2020). We discuss the validity of this
204 assumption in the discussion section. Finally, we compare the models to petrophysical
205 predictions for Earth properties in order to constrain temperature, the amount of partial
206 melt, and the amount of hydration, carbonization or sulfide weight percentage of the partial
207 melt in the asthenosphere.
208

209 Methods

210 MT data were inverted by Wang et al. (2020), which we briefly summarize here. The
211 determinant of the MT impedance tensor was used to invert logarithmic apparent resistivity
212 and linear phase along 2-D transects (line I and line II). The approach was chosen to
213 minimize 3-D coast effects from the nearby African coast (Wang et al., 2019). For the period
214 range chosen, 26–26,225 s, data quality and 3-D distortion were examined, and data points
215 with visible 3-D distortion were excluded in the inversions. The impedance polar diagrams of
216 the final selected data points were nearly parallel on either side of the Chain fracture zone
217 in lines I and II (Wang et al., 2020). Nevertheless, there may still be some 3-D effects due to
218 the fracture zones/3-D structure that influence the model, which we address in the
219 discussion section. Forward calculations and inversion were performed using the MAR2DEM
220 code (Key, 2016), modified to accept determinant data as an input (Wang et al., 2021).
221 Inversion of MT data with this approach is less dependent on the starting model than
222 surface wave inversion due to the diffusive nature of electromagnetic fields and the
223 smoothness and regularization of the inverse problem. Here we focus on varying the
224 starting model for the shear velocity inversion based on structural information from the
225 resistivity data, but not vice versa. We refer to this as resistivity structure guided shear
226 velocity inversion.
227

228 We first establish a relationship between shear velocity and resistivity in our study area. We
229 use two transects through the 3-D shear-wave velocity model of Harmon et al. (2020) in the
230 same locations of the two 2-D resistivity model transects of Wang et al. (2020). We make

231 cross-plots separately for the two lines. Cross-plots of the data suggest a linear relationship
232 between the two datasets, but with scatter (Fig. 3). The correlation coefficients of these
233 cross-plots for line I is 0.43 ± 0.01 and line II 0.39 ± 0.01 . A linear regression of line I between
234 shear-wave velocity (km/s) and resistivity ($\log_{10}(\rho)$), yields a solution of $V_s = 4.19 \pm 0.02 +$
235 $0.10 \pm 0.02 * \log_{10}(\rho)$, while for line II, $V_s = 4.22 \pm 0.02 + 0.08 \pm 0.02 * \log_{10}(\rho)$ and for line I and II
236 combined $V_s = 4.21 \pm 0.02 + 0.09 \pm 0.02 * \log_{10}(\rho)$.

237
238 We also consider predictions from laboratory petrophysical relationships between shear
239 velocity and resistivity for a half-space cooling model based on the error function solution to
240 the conductive heat transfer equation (Parker & Oldenburg, 1973; Turcotte & Schubert,
241 2002). To calculate the temperature structure, we assume a thermal diffusivity of 1×10^{-6}
242 $m^2 s^{-1}$, and a mantle potential temperature of $1350^\circ C$ calculated for seafloor age from 0-40
243 Myr, the approximate range in of ages along lines I and II (Fig. 4). To model the predicted
244 shear velocity for a given temperature, pressure, and melt fraction we use the Very
245 Broadband Rheology calculator (Havlin et al., 2021), assuming a peridotite mantle
246 composition. We use the attenuation parameterization of (Jackson & Faul, 2010) that is
247 included in the calculator and use an average across the surface wave period range used
248 here, 18-143 s period. In this model, the addition of melt primarily affects shear velocity
249 with ~2-4% velocity reduction for 1% melt volume fraction depending on the dihedral angle
250 (Takei, 1998). The model of Takei (1998) assumes that melt is interconnected, without
251 necessarily proscribing a melt geometry. The associated predicted velocity reduction
252 depends on wetness, which is a measure of the amount of grain to grain contact relative to
253 the melt (Takei, 1998). Other models for the effect of melt on velocity exist based on
254 different assumptions of melt geometry (Clark & Lesher, 2017; Hammond & Humphreys,
255 2000; Schmeling, 1985) which we evaluate in the discussion section. For resistivity we use
256 the relationship for hydrated mantle peridotite (Gardés et al., 2014) and a model for the
257 conductivity of hydrous mantle melts (Ni et al., 2011). We then use the Hashin-Shtrikman
258 upper bound to calculate the total resistivity of a melt bearing peridotite mantle (Ni et al.,
259 2011), which, again, assumes interconnected melt. The predictions for an example case with
260 100 ppm water content in the background mantle and 1% melt in the melt triangle and
261 variable amounts of water in the melt from 4-20 weight % are shown in Figure 4. We
262 perform a linear regression on the melt-free mantle data points (black dots, Fig. 4), and find
263 a relationship of $V_s = 4.14 \pm 0.02 + 0.11 \pm 0.01 * \log_{10}(\rho)$. This relationship is very similar to the
264 one derived for the cross-plot in line I; the velocity intercept is 0.05-0.06 km/s lower than in
265 our cross-plot, and the slope is only 0.01 km/s/ $\log_{10}(\rho)$ higher than in the cross-plot. Given
266 the similarity between the two and that the petrophysical line visually fits the data from the
267 shear velocity and resistivity inversions, we opt to use the relationship from the
268 petrophysical modelling.

269
270 We use the aforementioned petrophysical relationship to translate the resistivity model
271 (Fig. 2a, b) to shear-wave velocity, creating a new starting model (Fig. 5c, d) for the shear
272 velocity inversion. We then invert the phase velocities from 18-143 s period from Harmon et
273 al. (2020) sampled along lines I and II, for shear velocity as a function of depth, sampling at
274 every point, 0.1° . We calculate the partial derivatives relating Rayleigh wave phase velocity
275 to shear velocity using the Computer Programs in Seismology package (Herrmann, 2013),
276 and we assume a fixed V_p/V_s ratio of 1.8, which is consistent with the Preliminary Earth
277 Reference Model (PREM), a global one-dimensional (1-D) seismic velocity model

(Dziewonski & Anderson, 1981). We include a seawater layer along lines I and II in the model based on the local bathymetry. We use a damped least-squares inversion and assume an *a priori* model error of 0.2 km/s following choices from previous work (Forsyth & Li, 2005; Harmon et al., 2020). We replace the upper 5 km of the model beneath the water layer with average crustal values (3.5 km/s) from the 1-D model of Harmon et al. (2020). The model is parameterized every 5 km in depth down to 400 km. This parameterization is finer than that presented in Harmon et al. (2020) (Fig. 2). The finer parameterisation is necessary to capture the smaller scale variations in the resistivity model. Therefore, we also present an inversion using the 1-D starting model used in Harmon et al. (2020), but with the 5 km thick layers down to 400 km depth used here for comparison purposes (Fig. 5).

We next determine the physical properties that explain the resulting anomalies including temperature, melt fraction and volatile content of the melt. These quantities can trade off with each other, and multiple combinations can fit the data, and therefore we use a grid search approach. We presume that the thermal structure at any given point along each line is similar to the predicted thermal structure from the half space cooling model calculated above, but allow the effective seafloor age and corresponding thermal structure, resistivity and shear velocity to vary. The effective age of the seafloor (e.g. lithospheric thickness) could be greater due to “drips” (as in anomaly D) or younger if the lithosphere is thinned due to upwelling. In other words, although seafloor age is known at each profile, we search over the effective age of the seafloor given that our previously published models suggest that the age progression of the lithosphere might not be monotonic everywhere. We calculate the half space cooling thermal structure for seafloor from 0 to 40 Myr age in 1 Myr intervals as described above. The thermal models have an adiabatic gradient added to them, and as above, we assume a mantle potential temperature of 1350 °C. We did not vary the mantle potential temperature to minimize the free parameters in the grid search. Then, for each thermal structure from 0 to 40 Myr seafloor, we calculate the predicted shear velocity and resistivity for melt fractions from 0.00 to 0.07 at 0.001 increments below 0.01 and 0.005 increment above 0.01 and melt water contents from 0 to 30 weight % in 1% increments for all temperatures > 1100 °C at the corresponding depth/pressure values using the relationships described above for the half-space cooling model presented in Fig 4. We then examine the regions that cannot be explained by temperature alone, specifically, where the shear velocity is <4.4 km/s and \log_{10} resistivity is < 1.5 (< 30 Ωm), which are the nominal limits of the melt free predictions of the half-space cooling model (black dots, Fig 4). We perform a grid search over melt fraction, melt water content, and apparent seafloor age/temperature for each point in lines I and II. We then determine the chi-squared residual between the observed resistivity and shear velocity with the predicted resistivity and shear velocity at the same depth in each thermal structure from 0 to 40 Myr. The chi-squared residual is used to determine goodness of fit assuming an *a priori* standard deviation of 0.05 km/s for the shear velocity model and 0.10 $\log_{10}(\Omega\text{m})$ for the resistivity model. A value of melt, melt hydration and temperature is considered acceptable if the chi-squared value is < 1 for both the shear velocity and resistivity data. For most points, there are many combinations of melt, melt hydration and temperature that satisfactorily fit the data. The optimum value is the minimum summed value of the chi-squared values for resistivity and shear velocity. We present the error as the maximum parameter value minus the minimum acceptable parameter value divided by 2 for melt, melt water content and temperature,

324 which is the 95% confidence limit assuming symmetric error surfaces. We acknowledge that
325 this choice of reporting does not give a sense of the trade-offs in these parameters.
326

327 Results

328 The shear-wave velocity structure derived from translating the MT models to seismic
329 velocity according to the petrophysical predictions (Fig. 5c, d) closely resembles the MT
330 models (Fig. 2 a, b), which is to be expected. We impose a water layer of 0.0 km/s in the
331 model. The seismic velocities range from 4.5 km/s in the upper 20-50 km of the Earth, with a
332 minimum of 4.03 km/s associated with the lowest resistivity regions. Strong lateral
333 gradients are also visible in the starting model, with changes of 0.4 km/s over less than 50
334 km, particularly near anomaly C. The line II model has low velocity channels across the
335 transect at 20-70 km depth and several high velocity regions in the asthenospheric mantle.
336

337 When we use the shear-velocity model derived from MT (Fig. 5c, d) as the starting model for
338 the surface wave inversion we find a new shear-wave velocity model (Fig. 5 e, f) that more
339 closely resembles the MT models than the previously published model (Fig. 2). The highest
340 velocities are up to 4.81 km/s found in the fast lid, while the minimum velocity is 4.00 km/s,
341 found in anomaly B. The high velocity lid is more continuous than in the starting model but
342 follows a similar pattern of increasing thickness away from the ridges in both lines I and II. In
343 the asthenosphere, low velocity structures from the starting model are also retained.

344 Specifically, the channel structures in line II, near anomaly E and F, are retained throughout
345 much of the model, particularly in the east near anomaly F, with similar velocities (~4.0
346 km/s) to the starting model. The deep low velocity anomalies beneath anomaly E are also
347 retained in the final model. Anomaly E from the model of Harmon et al. (2020), has been
348 moved deeper into the mantle in the MT-derived starting model inversion, while anomaly F
349 has been compressed into the channel structure. In line I anomalies B and C are preserved
350 i.e., ~4.0 km/s from the starting model. Anomaly A is more pervasive beneath the ridge than
351 in the MT starting model. Anomaly D is also enhanced in the shear velocity model, with a
352 high velocity of 4.56 km/s relative to the starting model of 4.31 km/s at 100 km depth. The
353 chi-squared values indicating goodness of fit to the data are shown in Fig. 5a and 5b and are
354 ~1 or less for most of the profile indicating a fit that is within error. This goodness of fit is
355 similar to the values from Harmon et al. (2020).

356
357 When we use the 1-D starting model from Harmon et al. (2020) for the surface wave
358 inversion, and the parameterisation and damping used here we find similarities and
359 differences in comparison to Harmon et al. (2020) that illustrate the range of possible
360 models that fit the data (Fig. 5g, h). A high velocity lid is visible beneath the ridge and across
361 the region that ranges from 20-60 km in thickness. It shows low velocities beneath the ridge,
362 with a stronger and shallower low velocity region beneath the ridge than in the model of
363 Harmon et al. (2020), although in general the features are similar, and the magnitude of the
364 named velocity anomalies are similar in general, < 4.2 km/s but > 4.0 km/s. These
365 differences highlight the effect that even small changes in parameterization can have on the
366 final model. The normalized chi-squared fit to the data is shown in Fig. 5 a,b for Line I and II,
367 respectively. The chi-squared values are generally ~1 or less indicating that the model fits
368 the data within error and has a similar fit to the model with the MT starting model. It is
369 interesting to note, that prior to inversion (i.e., the 0th iteration), the fit of the 1-D model is

370 generally better than the MT starting model (chi-squared of ~2-3 vs 4-5, blue dashed v.s.
371 black dashed Fig. 5 a,b). This is likely because the 1-D model originated from the best fit 1-D
372 average seismic model for the region. Both converge to very similar final chi-squared values
373 after the iterative inversion. The new shear-velocity model with the 1-D starting model
374 presented in Figure 5g, h is primarily for comparison purposes. The goal of the paper is to
375 align the previously published shear-wave velocity and resistivity models, and so we do not
376 discuss the model of Figure 5g, h further except for the purposes of resolution discussions.
377

378 The correlation between resistivity and shear-velocity after inversion is higher when the MT
379 derived starting model is used in comparison to when the 1-D starting model is used. For
380 the 1-D starting model inversion result with the finer parameterization used here, there is a
381 slope visible in line I (Fig. 6a), but there is less of a visible relationship in line II (Fig 6b).
382 Visually, the cross-plots for the MT derived starting model inversion result are more linear,
383 with more of a slope visible in both lines I and II (Fig. 6 c, d). The correlation coefficients
384 between the resistivity model and the shear velocity model assuming 1-D starting model
385 presented here are 0.41 ± 0.01 and 0.29 ± 0.01 for lines I and II, in other words similar to that
386 between the resistivity and the original shear velocity model presented in Harmon 2020
387 above (0.43 ± 0.01 and 0.39 ± 0.01 respectively). The correlation coefficients are higher,
388 0.56 ± 0.01 and 0.62 ± 0.01 for lines I and II respectively, for the shear-wave model resulting
389 from the MT-derived starting model. With the two lines combined the correlation
390 coefficient is 0.60 ± 0.01 (Fig. 7).

391
392 We illustrate the behaviour of the effect of varying the amounts of melt and water in the
393 partial melt and compare it to the V_s and resistivity histogram for both lines I and II (Fig. 7).
394 We use the thermal structure from the half-space cooling model shown in Fig. 4 but now
395 allow partial melt at 0.1%, 1.0% and 3.0% where the mantle temperature exceeds 1100 °C.
396 We also vary the amount water in the partial melt between 4-20%. The smallest amount of
397 partial melt reduces the seismic velocity by << 1% in most cases, while the resistivity is
398 reduced by $\sim 0.6 \log_{10}(\Omega m)$ over the range of water contents presented here. At 1% melt the
399 shear velocity is reduced by ~2%, and the effect of increased water content is stronger,
400 reducing the resistivity up to $\sim 1.5 \log_{10}(\Omega m)$ at the highest water contents. Finally, at 3%
401 melt, the velocity is reduced by 4-5% and the resistivity reduction is up to $\sim 2.1 \log_{10}(\Omega m)$.
402 The span of partial melt and melt water contents considered here also generally spans the
403 range of most of the shear velocity and resistivity values from our inversions, i.e., the
404 petrophysical values overlie the peak in the histogram. There is a slight bias in the seismic
405 velocities with a longer tail towards higher values.

406
407 Given the good general agreement between the petrophysical modelling and the shear
408 velocity and resistivity model values, we map the amount of partial melt, water content of
409 the melt, and temperature relative to the half-space cooling model onto the transects of
410 lines I and II (Fig. 8). We only perform this mapping where shear velocity is < 4.4 km/s and
411 $\log_{10}(\rho) < 1.5 \log_{10}(\Omega m)$, which is the nominal lower limit of the melt free half-space cooling
412 model (Fig. 4 and Fig. 7). In line I we find partial melt contents up to 4-4.5% near anomalies
413 B and C and similar maximum values in line II for anomalies E and F. Lower values of partial
414 melt <2% are needed near anomaly A and for most of the other regions, typically requiring <
415 1%. The water content of the melts is typically < 10 weight % for most (~60 %) of the total
416 anomaly area (colored regions in Fig. 8), with the notable exception of anomaly C which

417 requires up to 24 weight % water content to account for the low resistivity found in this
418 region and anomaly B which requires up to 15 weight %. There are other smaller patches of
419 high-water content visible near the edges of some of the regions, and within the channel of
420 anomaly E. The temperature structure generally has cooler temperatures 1100-1200 °C at
421 depths < 100 km and temperatures > 1300 °C at greater depth. The grid search provides
422 formal error bounds corresponding to our presumed data errors (Fig. 9). The errors for the
423 melt percentages are typically <1%, while error for water content of the melt is on average 4
424 weight %, and the average errors for temperature are 26 °C.

425 Discussion

426 The inversion result from the MT derived starting model fits the phase velocity data within
427 error. Initially, the misfit of the MT-derived starting model before inversion is only a factor
428 of 2 greater than the misfit of the 1-D starting model before inversion in most places. This
429 suggests general agreement between the MT-derived starting model and the phase velocity
430 data. The inversion result using the MT-derived starting model fits the phase velocity data
431 just as well as the shear velocity model of Harmon et al. (2020) which used a 1-D starting
432 model and also the shear velocity model using the 1-D starting model and the finer
433 parameterisation presented here for comparison purposes. All of these have a normalized
434 chi-squared value 1 or less for most of the transects. The MT-derived shear-velocity model
435 improved the visual agreement and correlation coefficient between the resistivity and shear
436 velocity model.

437 Overall, many of the common features of the original studies are retained and several of the
438 anomalies come into better agreement. For example, the MT-derived shear velocity model
439 retains the thickening of the lithosphere and the drip feature at anomaly D observed in the
440 Harmon et al. (2020) model. The lithospheric thickening with distance from the ridge is
441 more pronounced in the MT-derived shear velocity model in comparison to that of Harmon
442 et al. (2020), presumably a result of removing the 1-D influence on the model. Anomalies B
443 and C are also retained in the MT-derived model, although anomaly B is more prominent
444 than in the Harmon et al. (2020) study. In the asthenosphere, better agreement between
445 the resistivity model and the MT-derived shear velocity model is achieved for the channel
446 features in line II associated with anomaly F. Anomaly C in the MT-derived shear velocity
447 model has a morphology more similar to the MT model than in the Harmon et al. (2020)
448 model. Other anomalies such anomaly A shifts shallower than the Harmon et al. (2020)
449 model and align better with a weak shallow anomaly directly beneath the ridge in the
450 resistivity model. Anomaly E is deeper than that in the Harmon et al. (2020) model, again in
451 better agreement with the resistivity model.

452
453 The differences in the shear velocity models here highlight some of the limitations of the
454 approach. Specifically, inversion of Rayleigh wave phase velocities for shear velocity
455 structure is non-unique, and this is well-known (Rychert et al., 2020) as many previous
456 works have demonstrated that a variety of models can fit a given dispersion curve. The
457 differences between Harmon et al. (2020) (Fig. 2), the 1-D starting model with smoothing,
458 damping, and parameterization of this study (Fig. 5e, f) and the MT-derived starting model
459 (Fig. 5g, h) illustrate this fact again and highlight that the strength of an anomaly can vary
460 from model to model depending on the starting model, even if similar damping is used and
461 the same fit is achieved as was the case here. For instance, the MT-derived shear-wave

463 velocity model includes velocities in Anomalies B, C that are up to 1% slower in comparison
464 with Harmon et al. (2020), which impacts interpretation in terms of the presence of partial
465 melt. Suitable additional constraints are needed to determine which structure is the most
466 likely, such as information from receiver functions or resistivity.

467

468 The cross-plots indicate that the shear-wave velocity model and resistivity are in good
469 agreement with the petrophysics predictions for the half-space cooling model and variable
470 partial melt concentrations and melt water contents. About 80% of the shear velocity data
471 lie within 0.1 km/s of the petrophysical predictions for reasonable temperature structure,
472 melt and melt water contents (Fig. 7). The resistivity model is completely spanned by the
473 petrophysical predictions. Shear velocity appears to be biased towards higher values, which
474 may be a result of either the inversion process or a physical process. Shear-wave velocity
475 inversions can trade off velocities at shallow depths with deeper asthenospheric anomalies,
476 by compensating low asthenospheric values with higher lithospheric values. On the other
477 hand, other physical effects such as depletion (Schutt & Lesher, 2006) of peridotite through
478 ridge melting toward more harzburgitic compositions (Hacker & Abers, 2004) could cause
479 higher velocities by ~1-2%. In addition, anisotropy could also enhance the apparent velocity
480 by up to 1-3% (Rychert & Harmon, 2017; Saikia et al., 2021). In reality, it is likely some
481 combination of these physical effects and model artefacts which are not accounted for in
482 the calculations used for predicting shear velocities.

483

484 In this work we chose to force the shear velocity structure towards a closer match to the
485 resistivity model, because the MT method has better resolution for certain features such as
486 electrically conductive thin channels, which is an assumption that is worth examination. We
487 presumed the resistivity model has better structural resolution, but this assumption has
488 limitations, since the 2-D assumption for the resistivity model may break down. For
489 instance, anomaly E is part of a larger 3-D velocity anomaly that extends to the south along
490 the Mid-Atlantic Ridge in Harmon et al. (2020), and the depth of the anomaly is much
491 greater in the resistivity anomaly, perhaps owing to issues of dimensionality. The deep
492 conductive anomalies beneath anomaly E are also poorly resolved in the MT data (Wang et
493 al., 2020), suggesting there is still some uncertainty about this particular location. Other
494 observations, such as S-to-P receiver functions, suggest there may be a shallower shear
495 velocity anomaly associated with anomaly E, which is necessary in order to produce a sharp
496 velocity contrast in these regions (Rychert et al., 2021). In addition, the lateral extent of the
497 S-to-P discontinuity agrees well with the lateral extent of the Harmon et al. (2020)
498 anomalies, suggesting this is a 3-D feature that is not well resolved in the 2-D MT inversion.
499 However, given that we prefer the MT-derived shear-wave velocity structure for some of
500 the major anomalies (A, B, C, D, and F), we proceed by interpreting our estimates for mantle
501 melting and melt water content, bearing the limitations of the inversions in mind.

502

503 The thermal structure predicted from our grid search (Fig. 8e, f) suggests relatively warm
504 temperatures beneath Anomalies B and C as well as the deeper parts of E (>1300 °C), while
505 Anomalies A and F have relatively low temperatures (1100-1200°C). This variability is likely a
506 result of the pressure dependence of the seismic waves. The low temperatures are generally
507 consistent with the interpretation that the shallow anomalies, particularly the channel
508 structures in F, are interacting with the base of the lithosphere (Harmon et al., 2020; Wang

509 et al., 2020). The deeper, hotter anomalies (anomaly B and C) are also generally consistent
510 with the interpretation of upwelling from depth associated with small scale convection.
511

512 The predicted melt fractions are in general agreement with our previous work from the
513 region, considering the various assumptions. Our melt fraction of up to 0.04 agrees with the
514 0.01 – 0.07 values previously reported based on the resistivity model alone (Wang et al.,
515 2020). It is higher than the 0.005 to 0.015 reported by the previous shear-wave velocity
516 model (Harmon et al., 2020). However, this can be explained by two main differences: 1)
517 The anomalies in the new shear velocity model presented here are up to 1 % slower than
518 those of the previous study (Harmon et al., 2020) and 2) We used the Takei (1998)
519 relationship between melt and velocity here, which corresponds to about a 2 % velocity
520 reduction for 0.01 melt fraction in comparison to the 7.9% reduction for 0.01 melt fraction
521 from the work of (Hammond & Humphreys, 2000) used by Harmon et al. (2020). Our melt
522 fraction result of up to 0.04 is also consistent with the 6 – 11 % velocity drop with depth
523 required by receiver functions after correcting for the maximum effect of temperature
524 (Rychert et al., 2021), which would require melt fractions of 0.03 – 0.06 assuming the same
525 melt-velocity relationship from Takei (1998) that we used here.

526

527 A different parameterization choice for the effects of melt on velocity due to different
528 assumptions on the melt geometry could yield lower melt fraction requirements by the
529 seismic constraints and still satisfy the resistivity model. The Takei (1998) model used here
530 presumes interconnected melt, which permits current flow and affects resistivity, but does
531 not prescribe a specific melt geometry rather using “wetness” and dihedral angle.
532 Unconnected melt geometries such as isolated pockets (Schmeling, 1985) do not affect
533 resistivity and so we can rule those out (Naif et al., 2021). Assuming interconnected films
534 and organized cuspatate tubules (Hammond & Humphreys, 2000), as used in Harmon et al.
535 (2020), reduces the maximum amount of partial melt fraction to < 0.02. Melt in the form of
536 interconnected tubules and cuspatate geometries (Hammond & Humphreys, 2000), which
537 have a velocity reduction of 14.5% per 0.01 melt fraction would suggest even lower melt
538 fractions (< 0.01). Resistivity does not depend strongly on the geometry of connected melt.
539 This is mostly due to the fact that the greatest resistivity reduction occurs at melt fractions <
540 0.03, with a more gradual reduction in resistivity at higher melt fractions (Fig. 10). However,
541 since resistivity also has a strong dependence on the volatile content in the melt, the lower
542 melt fractions predicted for the interconnected tubules and cuspatate geometries could also
543 satisfy the resistivity anomalies with additional volatiles. More work would be required to
544 determine the most likely partial melt geometry and relationship for shear velocity
545 reduction to place better constraints on the 3-fold variation predicted from differing
546 assumptions.

547

548 Predicted water contents are typically < 10 weight % for the melt but are surprisingly high,
549 up to weight 24%, in the centers of anomalies C and F. Simple fractional or batch melting
550 calculations suggest that for a typical MORB mantle source with 100 ppm and an average
551 6% melting of the mantle water contents of the melt should be ~0.2 weight % (Workman &
552 Hart, 2005). Higher water melt contents are possible for low degrees of partial melting, for
553 example <0.005 melt fraction yields > 1% weight water for 100 ppm in the mantle source,
554 and >7% weight water for 800 ppm in the mantle source. One possible explanation is that
555 these off-axis anomalies represent coalesced low-degree melts of a moderately wet mantle

556 with high water content. There is some geochemical evidence for a moderately wet mantle
557 from basalts collected from the ridge segments in the study area, with estimated water
558 contents that range from 110-770 ppm (~ 0.01-0.08 weight %) for the mantle source (Le
559 Voyer et al., 2015). The advantage of this model in which volatile rich melts coalesce is that
560 wet melts are stable and can persist in the mantle for long periods of time as has been
561 suggested as an explanation for inferred melt channels beneath older oceanic lithosphere
562 imaged by active source imaging (Mehouachi & Singh, 2018).

563
564 High CO₂ in the mantle melts instead of high-water content is another possible explanation
565 for the low resistivities observed in region (Sifre et al., 2014). Carbonated peridotite is
566 thought to exist in the mantle, although the abundance of carbon is relatively low, likely <
567 100 ppm, as it is present in ancillary phases, rather than being hosted in olivine or pyroxene
568 (Dasgupta & Hirschmann, 2010). Carbonated melts are generated and stable at greater
569 depths, and only small degrees of partial melt are likely to be generated (<0.001 melt
570 fraction) (Dasgupta & Hirschmann, 2010; Hirschmann, 2010). However, the melts could
571 percolate upwards and coalesce, generating higher CO₂ contents in the melt (Hirschmann,
572 2010). Fig. 10 shows the trade off in effective resistivity for 1 weight % water in the melt,
573 and 10% and 30% CO₂ by weight in the melt as a function of disequilibrium melt fraction
574 assuming 100 ppm in the un-melted mantle background for a depth of 80 km and a
575 temperature of 1350 °C. The figure is for demonstrative purposes since; (i) melt fraction is
576 imposed rather than generated using batch melting or fractional melting, (ii) we did not vary
577 temperature as we did in the silicate case, and (iii) the melt may not necessarily be stable.
578 At 30% CO₂ weight percent the resistivity is similar to the high-water content (20 weight %)
579 case. However, geochemical estimates of CO₂ in the primary ridge basalts range from 104
580 ppm to 1.9 weight % (Le Voyer et al., 2019), which is much lower than the >30 CO₂ weight %
581 needed to explain our results. To reach our high values, again aggregation of extremely low
582 degree partial melts would be required, and this also cannot be the melt that directly erupts
583 at the ridge.

584
585 Another possible explanation for the observed anomalies besides high water contents
586 (>10%) is sulfide melts, which are extremely conductive, >10⁴ S/m (Ducea & Park, 2000).
587 Small amounts of sulfide melts can rapidly reduce the effective resistivity of the aggregate.
588 To illustrate this we follow the parameterization of Ducea and Park (Ducea & Park, 2000),
589 using the (Gardés et al., 2014) parameterizations for the solid olivine and the Ni et al. (2011)
590 parameterization for the silicate melt. We assume a conductivity of 10⁴ S/m for sulfide
591 melts. Fig. 10 shows a comparison between the effective resistivity for an olivine matrix
592 with wet disequilibrium melts and also for sulfide/wet disequilibrium melt mixtures with
593 predominately sulfide melt. Like the CO₂ case, this is for demonstrative purposes, without
594 varying a full suite of parameters. A nearly pure sulfide melt has a similar resistivity as a
595 silicate melt with 20% water, reaching values below 1 Ωm at < 0.01 melt fraction. So, in this
596 case, regions of high melt water contents in Fig. 8, e.g., anomaly C, could also be regions of
597 high sulfide melt content. Given the bulk abundance of sulphur measured in basaltic glasses
598 in the region typically < 0.1 weight % (Le Voyer et al., 2015) and in <0.3 weight % in
599 xenoliths from continents (Ducea & Park, 2000), it is unlikely that 0.04-0.05 sulfide melt
600 fraction exists in the mantle. However, a more conservative sulfide melt fraction of ~0.01
601 could at least partially explain anomaly C (Hammond & Humphreys, 2000). There is also
602 some evidence that melts from the nearby ridge segments are sulphur saturated (Le Voyer

603 et al., 2015), and this may therefore suggest that sulfide melts may exist in higher
604 abundance away from the ridge melt triangle where silicate melts are in high abundance.
605 Sulfide melts have also been proposed to explain low seismic wave speeds in the
606 asthenosphere (Helffrich et al., 2011). Further work is needed to test whether sulfide melts
607 would be compatible with small scale convection and explain our off-axis anomalies, as they
608 have a higher density than silicate melts.

609
610 The melt anomalies inferred here extend to the base of our well-resolved region, ~150 km
611 depth, which is greater than the 60 – 80 km predictions of a dry melting curve (Katz et al.,
612 2003). This suggests that water or CO₂ induced melting is occurring at depth or the presence
613 of sulfide melts or some combinations are active to produce melts so deep. In addition, the
614 largest melt fractions are associated with anomalies B, C, E and F, which are far from the
615 ridge axis. This suggests melt generation occurs away from the ridge either owing to off-axis
616 small scale upwellings, the presence of volatiles, or the combination of the two. Persistent
617 melt near the base of the lithosphere and apparent channelization near anomaly F also
618 suggests a role for water or other volatiles in the melts in order to stabilize them at
619 relatively cool temperatures near the base of the lithosphere (Mehouachi & Singh, 2018).

620
621 Our joint seismic-MT constraints require melt fractions (> 0.01) over large swaths of the
622 asthenosphere mantle, several hundred kilometers, and hundreds of kilometers off the
623 ridge axis. Such high percentages are not expected to persist over time and length scales
624 that would enable seismic imaging (Spiegelman & Elliott, 1993). For instance, melt fractions
625 > 0.01 could be explained by a lack of a drainage route for the melt. Melt may coalesce at a
626 permeability boundary at the lithosphere-asthenosphere boundary, as suggested by recent
627 numerical models that include 2-phase flow (Sim et al., 2020). Asthenospheric porosity in
628 these models at a given snapshot in time can reach up to 10-20%, which could explain our
629 melt fraction observations in the channels (Sim et al., 2020). The melt may also reduce the
630 asthenospheric viscosity (Hirth & Kohlstedt, 1995; Jackson et al., 2006) potentially further
631 promoting small scale convection.

632
633 Partial melt is inferred in different geometries beneath the two different ridge segments in
634 our study region, including punctuated anomalous regions impinging on the base of the
635 plate, channels of melt beneath the plate, and punctuated regions at deeper depth.
636 Interestingly, the deeper melt exists at depths greater than predicted from simple adiabatic
637 upwelling models and are completely disconnected from the shallower melts. The variable
638 geometries may be related to the 3-D nature of the study area, and may also suggest that
639 we are imaging different stages in melt generation and migration, rather than steady-state
640 equilibrium melt. Our observations in light of these geodynamic models suggests that melt
641 is dynamic but may be persistent on geological timescales.

642 Conclusions

643 We developed a simple relationship for shear velocity and resistivity of the oceanic
644 lithosphere and asthenosphere that can be used to initialize these quantities for joint
645 inversions based on data from the I-LAB experiments and petrophysical modelling. We used
646 the relationship to create a shear-wave starting model that we used to re-invert the phase
647 velocities. The new shear-wave velocity model more closely resembles the resistivity
648 models, in particular by including a low velocity channel and also in terms of the location

649 and shape of slow velocity anomalies. The apparent lithospheric drip was also enhanced.
650 Overall, the correlation between the surface wave and MT datasets increased. This suggests
651 that apparent discrepancies between the original models are more likely an artefact of
652 resolution and inversion schemes. Surface waves cannot resolve thin channel structures
653 unless significant prior knowledge is used in the starting model in the inversion. We also
654 demonstrate the utility for shear velocity inversion guided by resistivity structure for mantle
655 melting and thermal structure based on petrophysical modelling. We show that shear
656 velocity can place good constraints on melt volume, while resistivity can place good
657 constraints on melt water content, CO₂ content or presence of sulfide melt given a simple
658 thermal structure such as the half-space cooling model.

659

660 Our estimates of melt, melt water content and temperature are in general reasonable and
661 within the expectations given geochemical outputs from the nearby ridge segments. The
662 one exception is very high water or CO₂ contents (>15%) estimated in the slowest and least
663 resistive anomalies. These high melt water or CO₂ contents could be real but would require
664 coalescing low degree partial melts of moderately wet or carbon-rich mantle sources.
665 Alternatively, nearly pure sulfide melts at small fractions could potentially partially explain
666 these anomalies. Overall, joint interpretation and/or inversion of resistivity and shear
667 velocity models holds promise for resolving debates about the lithosphere-asthenosphere
668 system and the presence and character of partial melt in the mantle.

669

670 Acknowledgements

671 C. A. R., N. H. and J. M. K. were funded by the Natural Environment Research Council
672 (NE/M003507/1 and NE/K010654/1) and the European Research Council (GA 638665). S. C.
673 was funded by the National Science Foundation under Grant OCE-1536400 (CA-LAB). S. W.
674 was funded by the Seafloor Electromagnetic Methods Consortium at Scripps Institution of
675 Oceanography and the Norwegian Research Council and the GAMES consortium at NTNU
676 (grant 294404). Seismic data are archived at the IRIS DMC, as 2016-2017 network XS
677 https://doi.org/10.7914/SN/XS_2016 (Rychert et al., 2016). We would also like to thank the
678 Associate Editor Max Moorkamp and two anonymous reviewers for their constructive
679 comments. We also thank the crews of RV Langseth (MGL2016-02) and RRS Discovery
680 (DY072) for their assistance with the data collection.

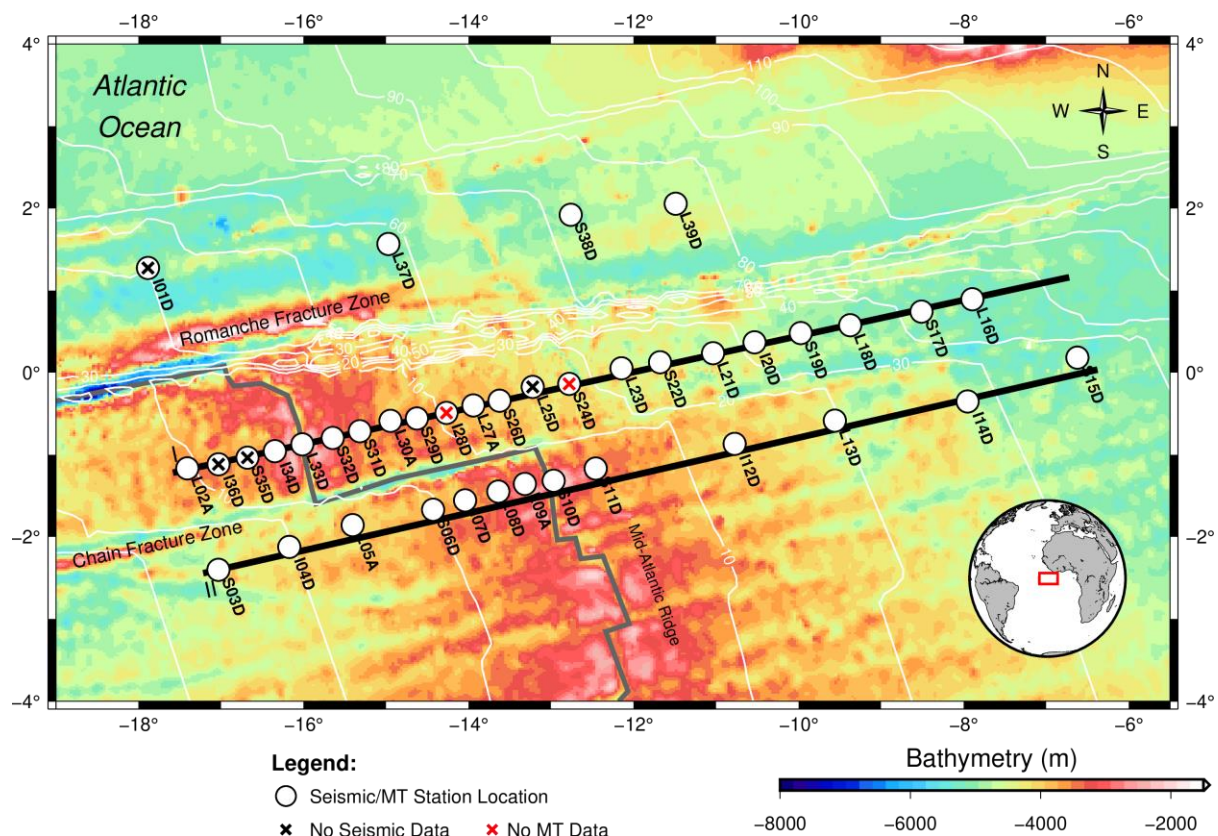
681

682

683

684 Figures

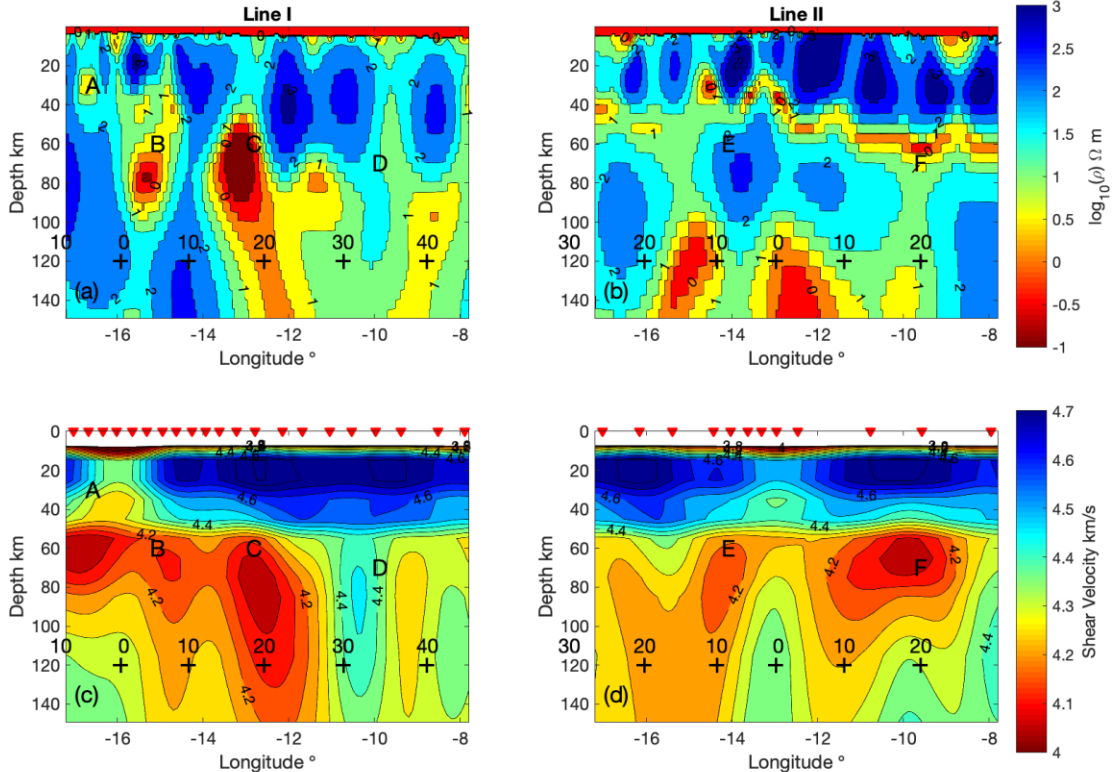
685



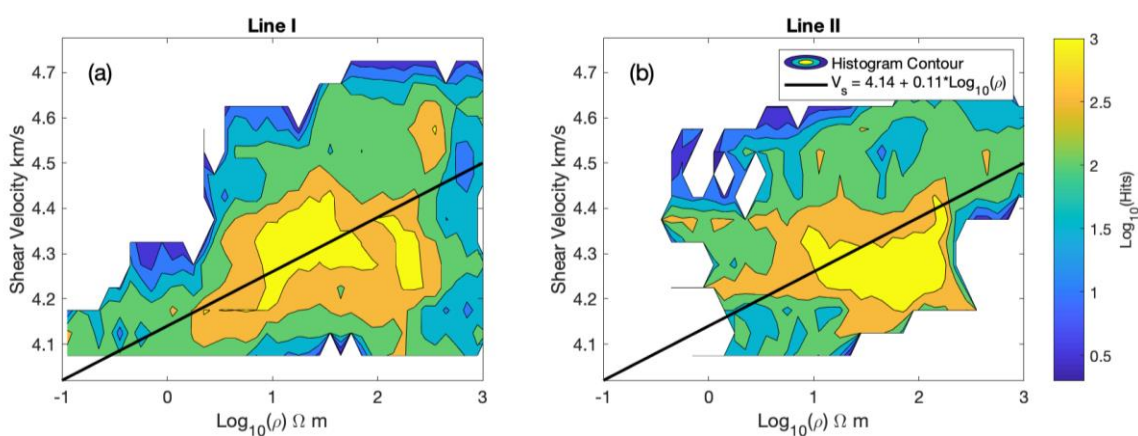
686

687

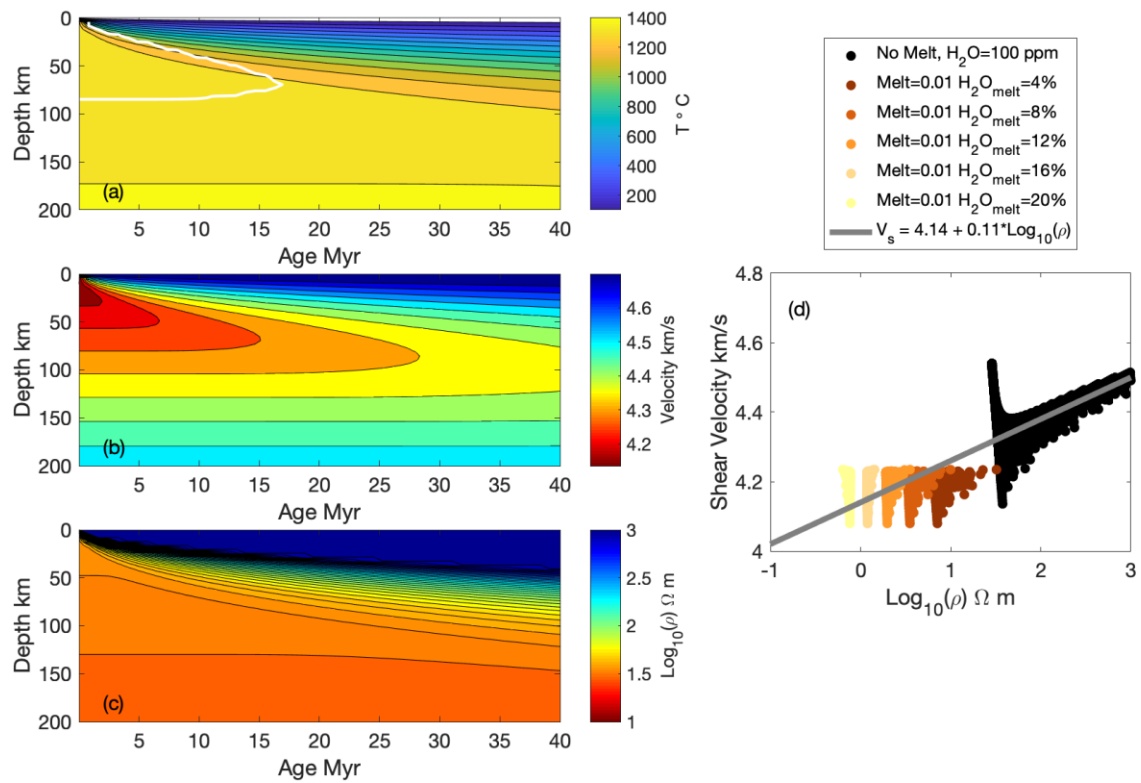
Figure 1. Map of the PI-LAB study region (Harmon et al., 2020). Circles indicate stations for seismic and MT locations with names indicated. MT stations are within 1-2 km of the seismic stations. Bold black lines I and II indicate transects used in this study. Background colors indicate bathymetry (Smith & Sandwell, 1997), white contours indicate seafloor age from Seton et al., (2020), and thick, dark grey line indicates the location of the Mid-Atlantic Ridge. Red box in inset map indicates study area.



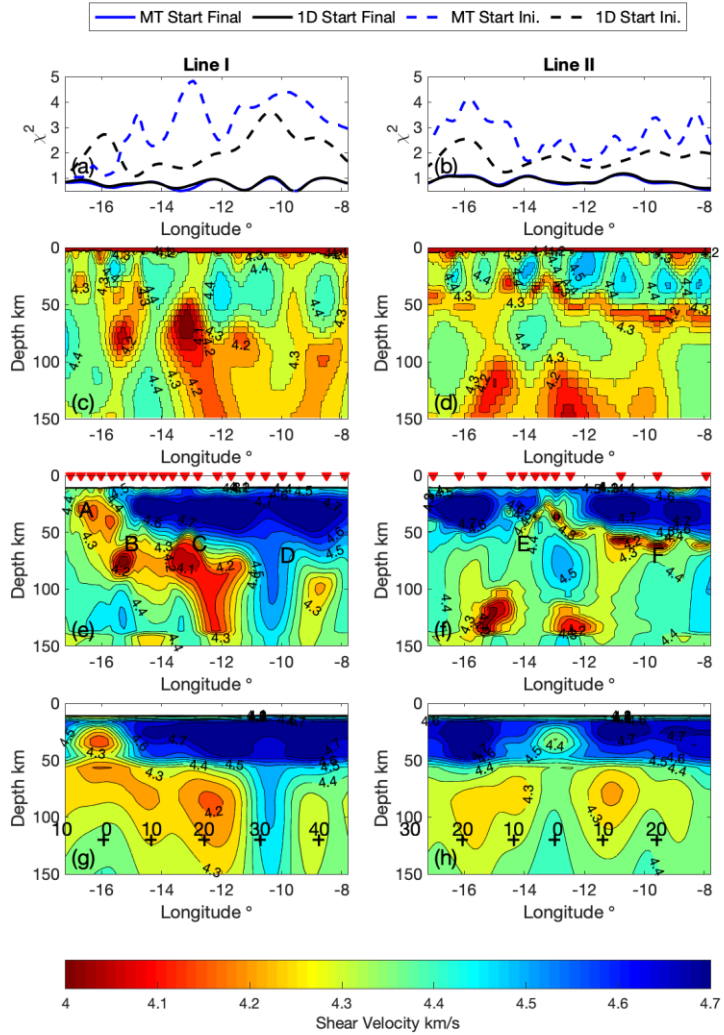
693
694 **Figure 2. Resistivity model and shear-wave velocity model from previous work.** Panels (a)
695 and (b) show contoured resistivity transects from line I and line II, respectively, from Wang
696 et al. (2020). Contour interval is 0.5 log units. Panels (c) and (d) show contoured shear
697 velocity transects for line I and II, respectively, from Harmon et al. (2020). Contour interval
698 is 0.05 km/s. Anomalies A, B, C, D, E and F from Harmon et al. (2020) are indicated. Red
699 triangles show seismic/MT station locations along the lines. Crosses at 120 km depth in plots
700 indicate the seafloor age, in Myr, with 0 indicating the ridge location.
701



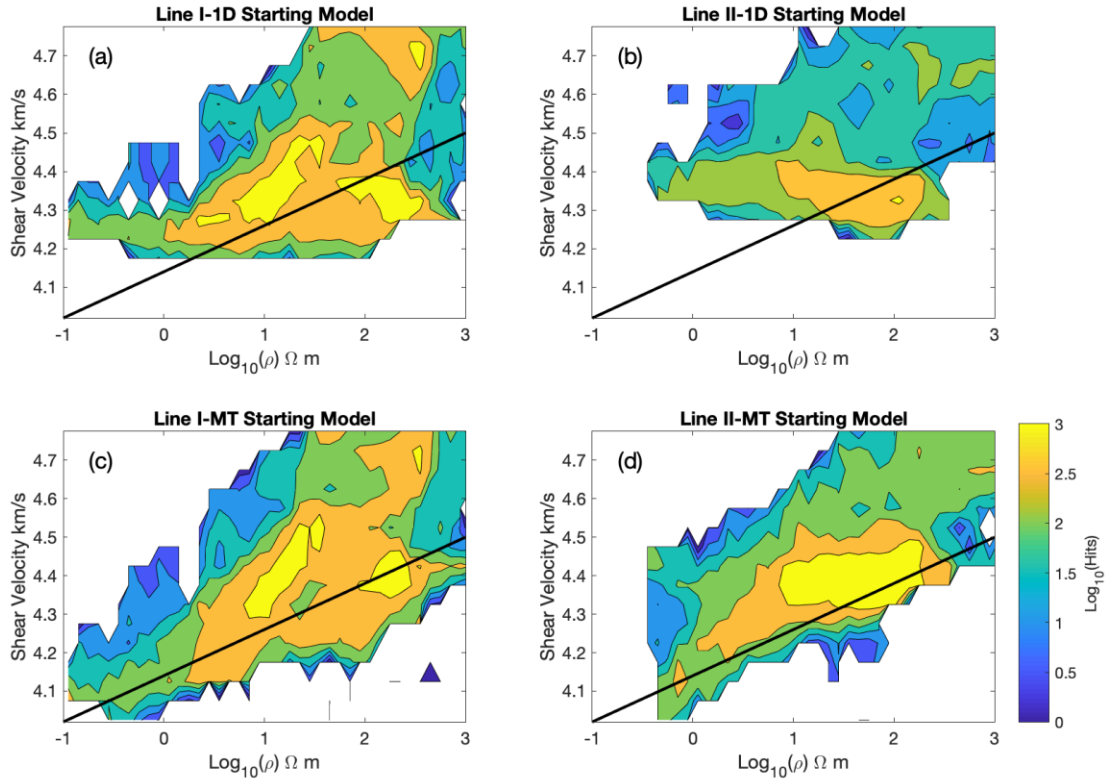
702
703 **Figure 3. Cross-plot histograms of resistivity and shear-wave velocity from previous work.**
704 Panels a and b shows the histograms for line I and line II, respectively. Black line indicates
705 preferred linear relationship from petrophysical modelling shown in Figure 4.



706
 707 **Figure 4. Petrophysical predictions for resistivity and shear-wave velocity for half-space**
 708 **cooling model.** Panel a shows the thermal structure for the half-space cooling model, b
 709 shows the predicted shear-wave velocity structure, and c shows the predicted resistivity
 710 structure predicted from petrophysics calculated as described in the text. White line in
 711 panel a indicates the predicted melt triangle for 100 ppm water in a background mantle
 712 (Katz et al., 2003). Panel d shows the cross-plot of predicted resistivity and shear velocity
 713 without melt from panel b and c (black circles) and with a presumed melt fraction (0.01)
 714 containing different amounts of water (4–20%), within the predicted melt triangle (yellow
 715 and brown circles). Grey line in Panel d shows preferred linear relationship between
 716 resistivity and shear velocity based petrophysical modelling presented here and consistent
 717 with the cross-plot histograms presented in Figure 3.



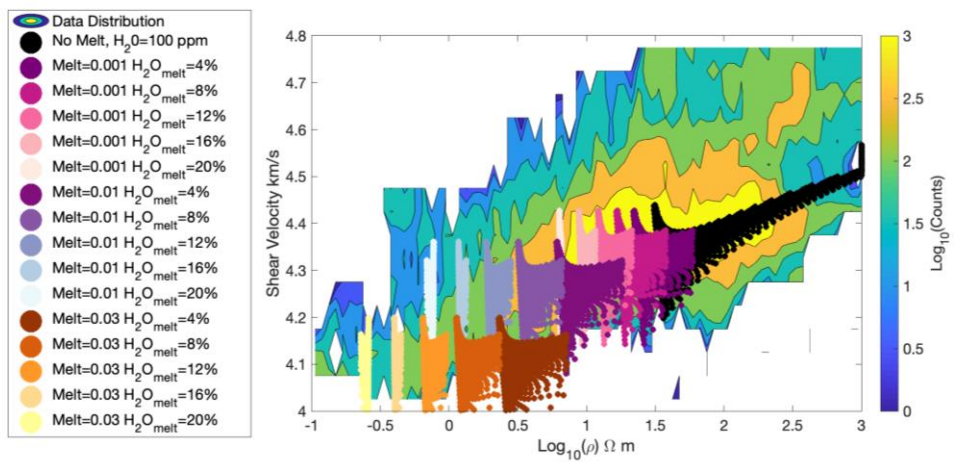
718
 719 **Figure 5. Shear-wave velocity inversions based on resistivity predictions.** Panels a and b
 720 show misfit along lines I and II using normalized chi-squared. Panels c and d show the shear-
 721 wave velocity models that result from translating the resistivity model shown in Fig. 2 to
 722 velocity using the linear relationships based on petrophysical modelling. Panels e and f show
 723 the shear-wave velocity inversion results using panels c and d, respectively, as starting
 724 models. Red triangles show seismic/MT station locations along the lines. Panels g and h show
 725 shear velocity inversion results using the 1-D starting model from Harmon et al. (2020)
 726 and the smoothing, damping, and model parameterisation used here. The model shown in
 727 panels g and h is for comparison purposes. It is different than that shown in Figure 2 panels
 728 c and d from Harmon et al. (2020) because we used a finer depth parameterisation here in
 729 order to capture the fine scale structure of the resistivity model. Contour interval is 0.05
 730 km/s. Asthenospheric anomalies A, B, C, D, E and F from Harmon et al. (2020) and Wang et
 731 al. (2020) are shown for reference. Crosses at 120 km depth in plots indicate the seafloor
 732 age, in Myr, with 0 indicating the ridge location.



733
 734 **Figure 6. Cross-plot histograms of resistivity and shear-wave velocity models.** Panels a and
 735 b show the cross-plot histograms for line I and line II, respectively, for the shear-wave
 736 velocity model derived from using the 1-D velocity starting model from Harmon et al. (2020)
 737 and the damping, smoothing, and parameterisation used here (Figure 5g, h). Panels c and d
 738 show the cross-plot histograms of the MT-derived shear-wave velocity model (Fig. 5 e, f).
 739 Black line indicates preferred linear relationship from petrophysical modelling shown in
 740 Figure 4.
 741
 742

743

744



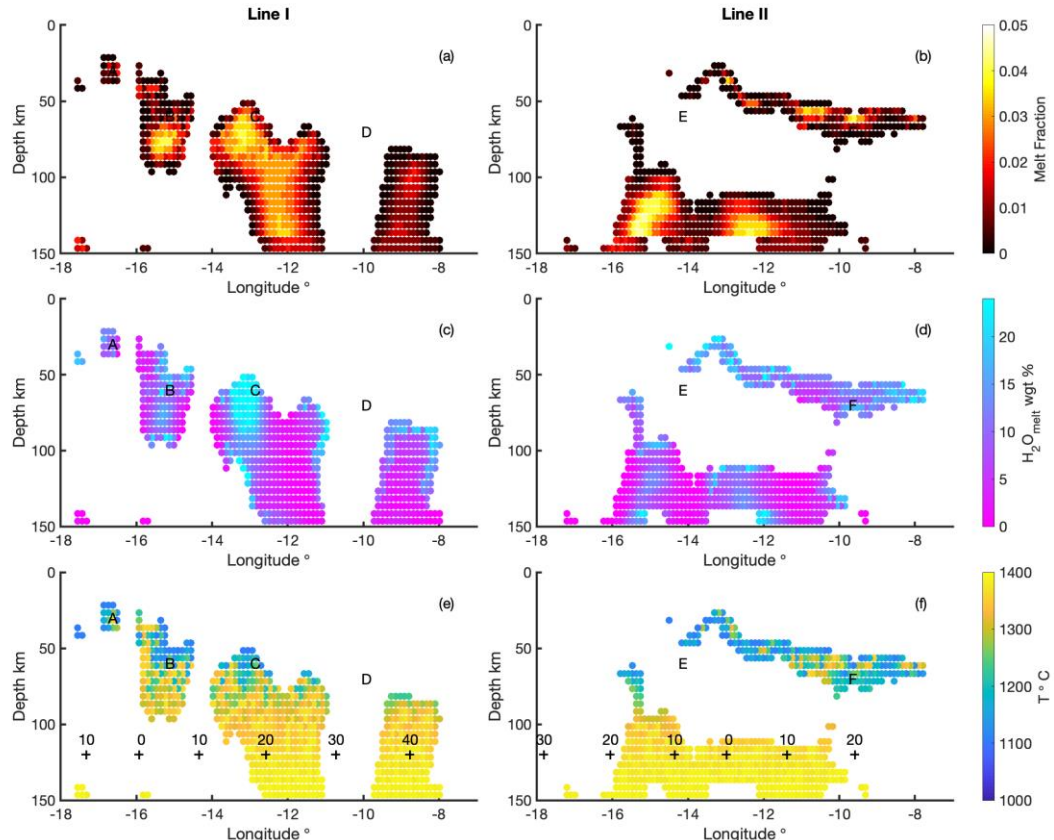
745

Figure 7. Cross-plot histogram of resistivity and shear-wave velocity from the MT-derived shear-wave velocity model for both lines I II and petrophysical predictions. Purely thermal predictions are shown as black dots. Colored dots show predictions for various melt fractions and melt water contents. Legend indicates the amount of imposed disequilibrium melt fraction (0.001, 0.01 and 0.03) and water content of the melt in weight % (4-20%).

751

752

753



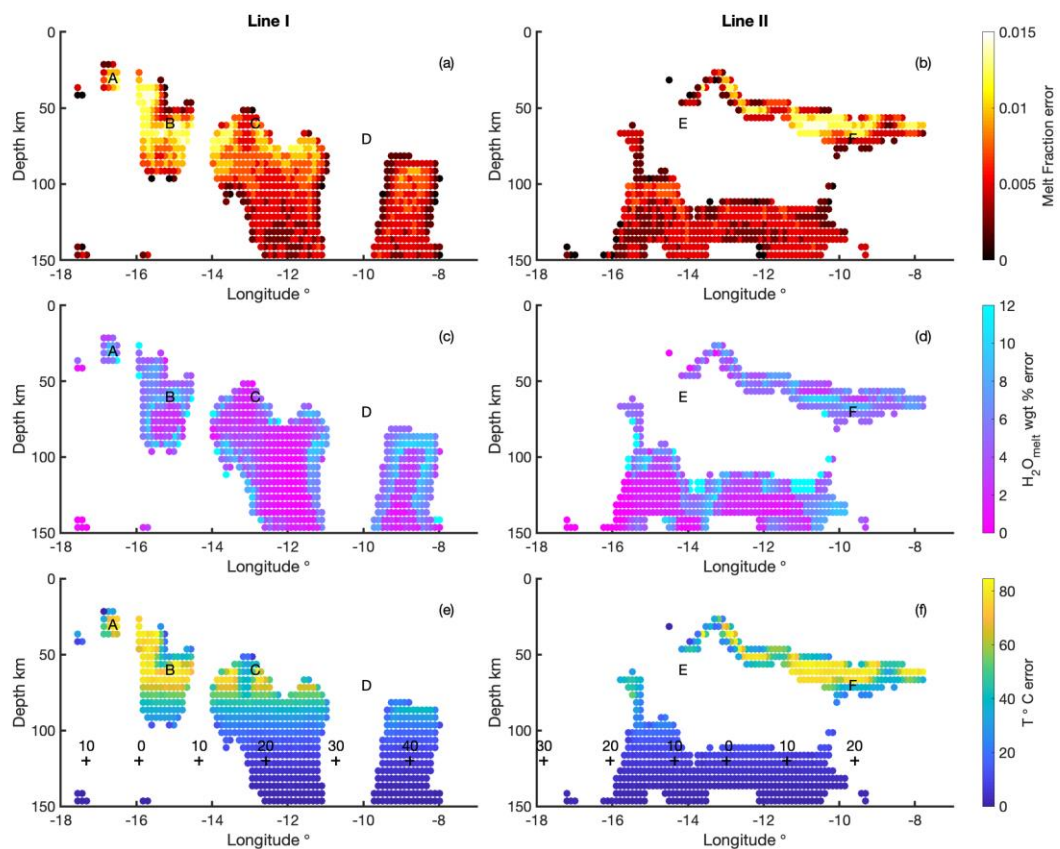
754

755

Figure 8. Results of grid search for partial melt, melt water content and mantle temperature. Panels a and b show results for partial melt fraction, panels c and d show water content of the partial melt, and panels e and f show the result for temperature for lines I and II, respectively. Anomalies A, B, C, D, E and F are plotted at the same locations as in Figure 2 for reference. Crosses at 120 km depth in plots indicate the seafloor age, in Myr, with 0 indicating the ridge location.

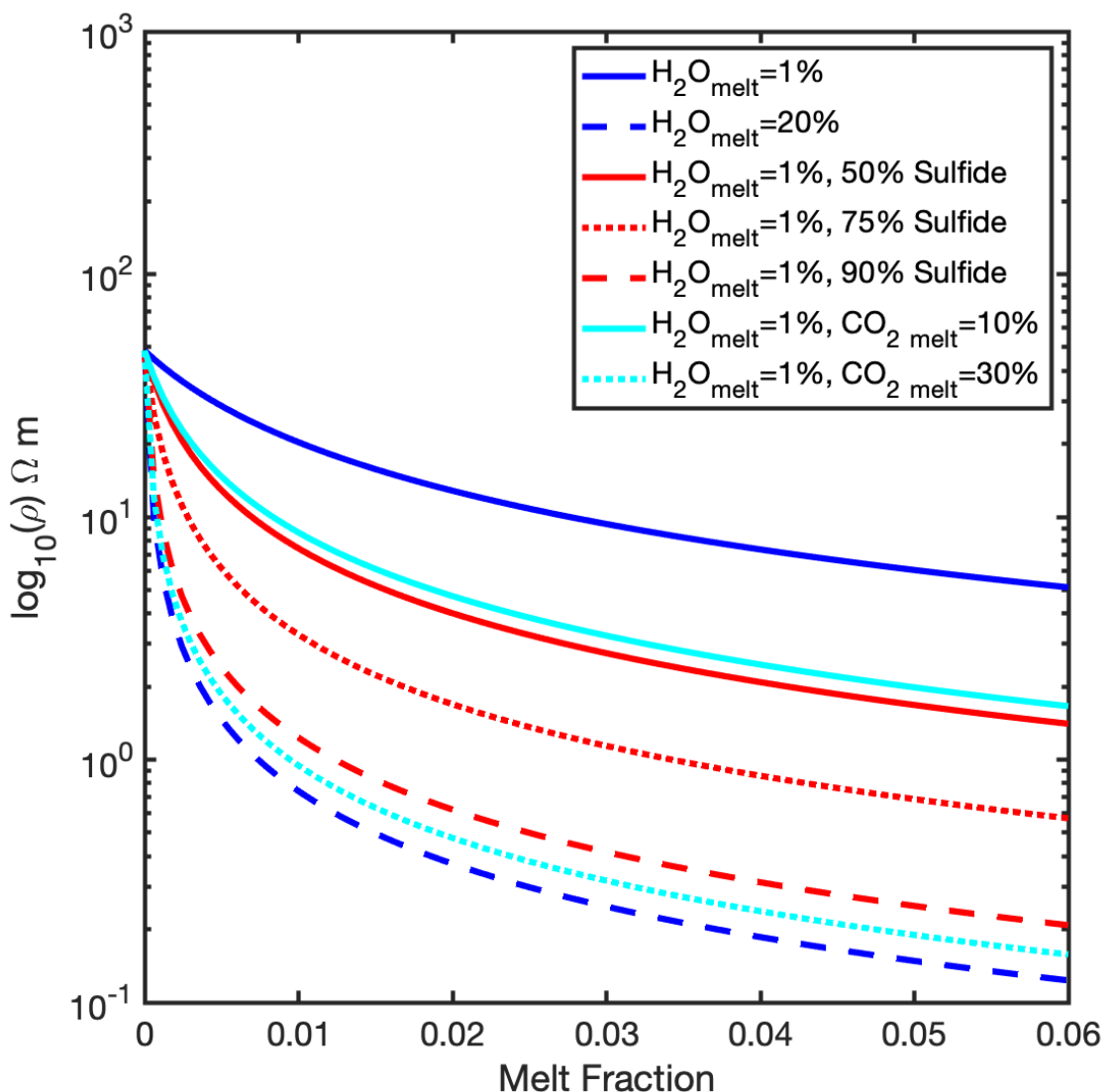
761

762



763
764
765
766
767
768
769
770

Figure 9. Error estimates of grid search for partial melt, water content of the melt and mantle temperature. Panels a and b show partial melt fraction error, panels c and d show water content of the partial melt error, and panels e and f show temperature error for line I and line II, respectively. Anomalies A, B, C, D, E and F are plotted at the same locations as in Figure 2 for reference. Crosses at 120 km depth in plots indicate the seafloor age, in Myr, with 0 indicating the ridge location.



771
 772 **Figure 10. Effective resistivity predictions for water, CO₂ and sulfide in silicate melts as a**
 773 **function of melt fraction.** We assume a solid mantle with 100 ppm water and disequilibrium
 774 melt at 1300°C. Legend indicates the respective water, CO₂ and sulfide concentrations. Melt
 775 with water only is shown as blue lines. Melt that includes water and CO₂ is shown as cyan
 776 lines and melt that includes sulfide is shown as red lines.
 777

778 References

- 779 Abers, G. A., Fischer, K. M., Hirth, G., Wiens, D. A., Plank, T., Holtzman, B. K., . . . Gazel, E.
780 (2014). Reconciling mantle attenuation-temperature relationships from seismology,
781 petrology, and laboratory measurements. *Geochemistry Geophysics Geosystems*,
782 15(9), 3521-3542. doi:10.1002/2014gc005444
- 783 Abubakar, A., Gao, G., Habashy, T. M., & Liu, J. (2012). Joint inversion approaches for
784 geophysical electromagnetic and elastic full-waveform data. *Inverse Problems*, 28(5).
785 doi:Artn 055016
786 10.1088/0266-5611/28/5/055016
- 787 Agius, M., Harmon, N., Rychert, C. A., Tharimena, S., & Kendall, J. M. (2018). Sediment
788 Characterization at the Equatorial Mid - Atlantic Ridge From P - to - S Teleseismic
789 Phase Conversions Recorded on the PI - LAB Experiment. *Geophysical Research
790 Letters*, 45. doi:<https://doi.org/10.1029/2018GL080565>
- 791 Anderson, D., & Sammis, C. (1970). Partial Melting in the Upper Mantle. *Phys. Earth Plan.
792 Interiors*, 3, 41-50.
- 793 Baba, K., Chave, A. D., Evans, R. L., Hirth, G., & Mackie, R. L. (2006). Mantle dynamics
794 beneath the East Pacific Rise at 17 degrees S: Insights from the Mantle
795 Electromagnetic and Tomography (MELT) experiment. *J. Geophys. Res.*, 111(B02101).
796 doi:doi:10.1029/2004JB003598
- 797 Bell, S., Ruan, Y. Y., & Forsyth, D. W. (2016). Ridge asymmetry and deep aqueous alteration
798 at the trench observed from Rayleigh wave tomography of the Juan de Fuca plate.
799 *Journal of Geophysical Research-Solid Earth*, 121(10), 7298-7321.
800 doi:10.1002/2016jb012990
- 801 Bennington, N. L., Zhang, H. J., Thurber, C. H., & Bedrosian, P. A. (2015). Joint Inversion of
802 Seismic and Magnetotelluric Data in the Parkfield Region of California Using the
803 Normalized Cross-Gradient Constraint. *Pure and Applied Geophysics*, 172(5), 1033-
804 1052. doi:10.1007/s00024-014-1002-9
- 805 Clark, A. N., & Lesher, C. E. (2017). Elastic properties of silicate melts: Implications for low
806 velocity zones at the lithosphere-asthenosphere boundary. *Science Advances*, 3(12).
- 807 Colombo, D., & Rovetta, D. (2018). Coupling strategies in multiparameter geophysical joint
808 inversion. *Geophys. J. Int.*, 215(2), 1171-1184. doi:10.1093/gji/ggy341
- 809 Dasgupta, R., & Hirschmann, M. M. (2010). The deep carbon cycle and melting in Earth's
810 interior. *Earth and Planetary Science Letters*, 298(1-2), 1-13.
811 doi:10.1016/j.epsl.2010.06.039
- 812 Ducea, M. N., & Park, S. K. (2000). Enhanced Mantle Conductivity from Sulfide Minerals,
813 Southern Sierra Nevada, California. *Geophysical Research Letters*, 27(16), 2405-2408.
814 doi:<https://doi.org/10.1029/2000GL011565>
- 815 Dunn, R. A., & Forsyth, D. W. (2003). Imaging the transition between the region of mantle
816 melt generation and the crustal magma chamber beneath the southern East Pacific
817 Rise with short-period Love waves. *J. Geophys. Res.*, 108(B7), 2352,
818 doi:2310.1029/2002JB002217.
- 819 Dziewonski, A. M., & Anderson, D. L. (1981). Preliminary Reference Earth Model. *Phys. Earth
820 Plan. Inter.*, 25(4), 297-356.
- 821 Evans, R. L., Tarits, P., Chave, A. D., White, A., Heinson, G., Filloux, J. H., . . . Unsworth, M. J.
822 (1999). Asymmetric electrical structure in the mantle beneath the East Pacific Rise at
823 17 degrees S. *Science*, 286(5440), 752-756.

- 824 Forsyth, D. W., & Li, A. (2005). Array-analysis of two-dimensional variations in surface wave
825 phase velocity and azimuthal anisotropy in the presence of multipathing
826 interference. In A. Levander & G. Nolet (Eds.), *Seismic Data Analysis and Imaging*
827 with Global and Local Arrays: AGU Monograph.
- 828 Forsyth, D. W., Scheirer, D. S., Webb, S. C., Dorman, L. M., Orcutt, J. A., Harding, A. J., . . .
829 Team, M. S. (1998). Imaging the deep seismic structure beneath a mid-ocean ridge:
830 The MELT experiment. *Science*, 280(5367), 1215-1218.
- 831 Frost, B. R., Fyfe, W. S., Tazaki, K., & Chan, T. (1989). Grain-Boundary Graphite in Rocks and
832 Implications for High Electrical-Conductivity in the Lower Crust. *Nature*, 340(6229),
833 134-136. doi:DOI 10.1038/340134a0
- 834 Gaherty, J. B., Jordan, T. H., & Gee, L. S. (1996). Seismic structure of the upper mantle in a
835 central Pacific corridor. *J. Geophys. Res.*, 101(B10), 22,291-222,309.
- 836 Gallardo, L. A., & Meju, M. A. (2004). Joint two-dimensional DC resistivity and seismic travel
837 time inversion with cross-gradients constraints. *Journal of Geophysical Research-Solid Earth*, 109(B3). doi:Artn B03311
838 10.1029/2003jb002716
- 840 Gao, H. Y. (2016). Seismic velocity structure of the Juan de Fuca and Gorda plates revealed
841 by a joint inversion of ambient noise and regional earthquakes. *Geophysical
842 Research Letters*, 43(10), 5194-5201. doi:10.1002/2016gl069381
- 843 Gardés, E., Gaillard, F., & Tarits, P. (2014). Toward a unified hydrous olivine electrical
844 conductivity law. *Geochemistry, Geophysics, Geosystems*, 15(12), 4984-5000.
845 doi:<https://doi.org/10.1002/2014GC005496>
- 846 Goetze, C., Poirier, J. P., Kelly, A., Cook, A. H., & Greenwood, G. W. (1978). The mechanisms
847 of creep in olivine. *Philosophical Transactions of the Royal Society of London. Series
848 A, Mathematical and Physical Sciences*, 288(1350), 99-119.
849 doi:doi:10.1098/rsta.1978.0008
- 850 Guo, R., Yao, H. M., Li, M., Ng, M. K. P., Jiang, L., & Abubakar, A. (2020). Joint Inversion of
851 Audio-Magnetotelluric and Seismic Travel Time Data With Deep Learning Constraint.
852 *IEEE Transactions on Geoscience and Remote Sensing*, 1-14.
853 doi:10.1109/TGRS.2020.3032743
- 854 Haber, E., & Oldenburg, D. (1997). Joint inversion: a structural approach. *Inverse Problems*,
855 13(1), 63-77. doi:10.1088/0266-5611/13/1/006
- 856 Hacker, B. R., & Abers, G. A. (2004). Subduction Factory 3: An Excel worksheet and macro for
857 calculating the densities, seismic wave speeds, and H₂O contents of minerals and
858 rocks at pressure and temperature. *Geochemistry Geophysics Geosystems*, 5.
859 doi:Artn Q01005,10.1029/2003gc000614
- 860 Hammond, W. C., & Humphreys, E. D. (2000). Upper mantle seismic wave velocity: Effects of
861 realistic partial melt geometries. *J. Geophys. Res.*, 105(5), 10975-10986.
- 862 Harmon, N., Rychert, C., Kendall, J., Tharimena, S., Bogiatzis, P., & Agius, M. (2020).
863 Evolution of the oceanic Lithosphere in the equatorial Atlantic from Rayleigh Wave
864 tomography, evidence for small-scale convection from the PI-LAB experiment.
865 *Geochem. Geophys. Geosys.*(10.1029/2020GC009174). doi:10.1029/2020GC009174
- 866 Harmon, N., Rychert, C. A., Agius, M. R., Tharimena, S., Le Bas, T. P., Kendall, J. M., &
867 Constable, S. (2018). Marine geophysical investigation of the Chain Fracture Zone in
868 the equatorial Atlantic from the PI-LAB Experiment. *J. Geophys. Res.*, 123, 11,016–
869 011,030. doi:10.1029/2018JB015982

- 870 Havlin, C., Holtzman, B., & Hopper, E. (2021). Inference of thermodynamic state in the
871 asthenosphere from anelastic properties, with applications to north American upper
872 mantle. *Phys. Earth Plan. Inter.*, 106639.
873 doi:<https://doi.org/10.1016/j.pepi.2020.106639>
- 874 Helffrich, G., Kendall, J.-M., Hammond, J. O. S., & Carroll, M. R. (2011). Sulfide melts and
875 long-term low seismic wavespeeds in lithospheric and asthenospheric mantle.
876 *Geophysical Research Letters*, 38(11). doi:<https://doi.org/10.1029/2011GL047126>
- 877 Herrmann, R. B. (2013). Computer Programs in Seismology: An Evolving Tool for Instruction
878 and Research. *Seismological Research Letters*, 84(6), 1081-1088.
879 doi:10.1785/0220110096
- 880 Hirschmann, M. M. (2010). Partial melt in the oceanic low velocity zone. *Phys. Earth Plan.*
881 *Inter.*, 179(1-2), 60-71. doi:10.1016/J.Pepi.2009.12.003
- 882 Hirth, G., & Kohlstedt, D. L. (1995). Experimental Constraints on the Dynamics of the
883 Partially Molten Upper-Mantle .2. Deformation in the Dislocation Creep Regime. *J.*
884 *Geophys. Res.*, 100(8), 15441-15449.
- 885 Jackson, I., & Faul, U. H. (2010). Grainsize-sensitive viscoelastic relaxation in olivine: Towards
886 a robust laboratory-based model for seismological application. *Phys. Earth Plan.*
887 *Inter.*, 183(1-2), 151-163. doi:Doi 10.1016/J.Pepi.2010.09.005
- 888 Jackson, I., Faul, U. H., Fitz Gerald, J. D., & Morris, S. J. S. (2006). Contrasting viscoelastic
889 behavior of melt-free and melt-bearing olivine: Implications for the nature of grain-
890 boundary sliding. *Materials Science and Engineering a-Structural Materials*
891 *Properties Microstructure and Processing*, 442(1-2), 170-174. doi:Doi
892 10.1016/J.Msea.2006.01.136
- 893 Jegen, M. D., Hobbs, R. W., Tarits, P., & Chave, A. (2009). Joint inversion of marine
894 magnetotelluric and gravity data incorporating seismic constraints: Preliminary
895 results of sub-basalt imaging off the Faroe Shelf. *Earth and Planetary Science Letters*,
896 282(1), 47-55. doi:<https://doi.org/10.1016/j.epsl.2009.02.018>
- 897 Johansen, S. E., Panzner, M., Mittet, R., Amundsen, H. E. F., Lim, A., Vik, E., . . . Arntsen, B.
898 (2019). Deep electrical imaging of the ultraslow-spreading Mohns Ridge. *Nature*,
899 567(7748), 379-. doi:10.1038/s41586-019-1010-0
- 900 Karato, S.-I. (2012). On the origin of the asthenosphere. *Earth Planet. Sci. Lett.*, 321-322, 95-
901 103.
- 902 Katz, R. F., Spiegelman, M., & Langmuir, C. H. (2003). A new parameterization of hydrous
903 mantle melting. *Geochem. Geophys. Geosys.*, 4(9), 1073,
904 doi:1010.1029/2002GC000433.
- 905 Kawakatsu, H., Kumar, P., Takei, Y., Shinohara, M., Kanazawa, T., Araki, E., & Suyehiro, K.
906 (2009). Seismic Evidence for Sharp Lithosphere-Asthenosphere Boundaries of
907 Oceanic Plates. *Science*, 324(5926), 499-502. doi:10.1126/science.1169499
- 908 Key, K. (2016). MARE2DEM: a 2-D inversion code for controlled-source electromagnetic and
909 magnetotelluric data. *Geophys. J. Int.*, 207(1), 571-588. doi:10.1093/gji/ggw290
- 910 Key, K., Constable, S., Liu, L., & Pommier, A. (2013). Electrical image of passive mantel
911 upwelling beneath the northern East Pacific Rise. *Nature*, 495, 499-502.
912 doi:doi:10.1038/nature11932
- 913 Le Voyer, M., Cottrell, E., Kelley, K. A., Brounce, M., & Hauri, E. H. (2015). The effect of
914 primary versus secondary processes on the volatile content of MORB glasses: An
915 example from the equatorial Mid-Atlantic Ridge (5 degrees N-3 degrees S). *Journal of*
916 *Geophysical Research-Solid Earth*, 120(1), 125-144. doi:10.1002/2014jb011160

- 917 Le Voyer, M., Hauri, E. H., Cottrell, E., Kelley, K. A., Salters, V. J. M., Langmuir, C. H., . . . Füri,
918 E. (2019). Carbon Fluxes and Primary Magma CO₂ Contents Along the Global Mid-
919 Ocean Ridge System. *Geochemistry, Geophysics, Geosystems*, 20(3), 1387-1424.
920 doi:<https://doi.org/10.1029/2018GC007630>
- 921 McKenzie, D., & Parker, R. (1967). The North Pacific: an Example of Tectonics on a Sphere.
922 *Nature*, 216, 1276–1280 doi:<https://doi.org/10.1038/2161276a0>
- 923 Mehouachi, F., & Singh, S. (2018). Water-rich sublithospheric melt channel in the equatorial
924 Atlantic Ocean. *Nat. Geosci.*, 11, 65-69. doi:doi:10.1038/s41561-017-0034-z
- 925 Moorkamp, M., Heincke, B., Jegen, M., Roberts, A. W., & Hobbs, R. W. (2011). A framework
926 for 3-D joint inversion of MT, gravity and seismic refraction data. *Geophys. J. Int.*,
927 184(1), 477-493. doi:10.1111/j.1365-246X.2010.04856.x
- 928 Moorkamp, M., Jones, A. G., & Fishwick, S. (2010). Joint inversion of receiver functions,
929 surface wave dispersion, and magnetotelluric data. *Journal of Geophysical Research-Solid Earth*,
930 115. doi:Artn B04318
931 10.1029/2009jb006369
- 932 Naif, S., Key, K., Constable, S., & Evans, R. L. (2013). Melt-rich channel observed at the
933 lithosphere-asthenosphere boundary. *Nature*, 495(7441), 356-359.
- 934 Naif, S., Selway, K., Murphy, B. S., Egbert, G., & Pommier, A. (2021). Electrical conductivity of
935 the lithosphere-asthenosphere system. *Phys. Earth Plan. Inter.*, 313, 106661.
936 doi:<https://doi.org/10.1016/j.pepi.2021.106661>
- 937 Ni, H., Keppler, H., & Behrens, H. (2011). Electrical conductivity of hydrous basaltic melts:
938 implications for partial melting in the upper mantle. *Contributions to Mineralogy and
939 Petrology*, 162(3), 637-650. doi:10.1007/s00410-011-0617-4
- 940 Parker, R. L., & Oldenburg, D. W. (1973). Thermal Model of Ocean Ridges. *Nature, Phys. Sci.*,
941 242(122), 137-139.
- 942 Priestley, K., & McKenzie, D. (2006). The thermal structure of the lithosphere from shear
943 wave velocities. *Earth Plan. Sci. Lett.*, 244(1-2), 285-301.
- 944 Rychert, C. A., Fischer, K. M., & Rondenay, S. (2005). A sharp lithosphere-asthenosphere
945 boundary imaged beneath eastern North America. *Nature*, 436(7050), 542-545.
- 946 Rychert, C. A., & Harmon, N. (2017). Constraints on the anisotropic contributions to velocity
947 discontinuities at ~60 km depth beneath the Pacific. *Geochemistry, Geophysics,
948 Geosystems*, 18. doi:10.1002/2017GC006850
- 949 Rychert, C. A., Harmon, N., Constable, S., & Wang, S. G. (2020). The Nature of the
950 Lithosphere-Asthenosphere Boundary. *Journal of Geophysical Research-Solid Earth*,
951 125(10). doi:ARTN e2018JB016463
952 10.1029/2018JB016463
- 953 Rychert, C. A., Harmon, N., & Tharimena, S. (2018). Seismic Imaging of the Base of the
954 Ocean Plates. In H. Yuan (Ed.), *Lithospheric Discontinuities* (pp. 71-87). Washington
955 DC: AGU Monographs.
- 956 Rychert, C. A., Kendall, J. M., & Harmon, N. (2016). *Passive Imaging of the Lithosphere-
957 Asthenosphere Boundary*.
- 958 Rychert, C. A., Rondenay, S., & Fischer, K. M. (2007). P-to-S and S-to-P imaging of a sharp
959 lithosphere-asthenosphere boundary beneath eastern North America. *Journal of
960 Geophysical Research-Solid Earth*, 112(B8). doi:Artn B08314
961 10.1029/2006jb004619

- 962 Rychert, C. A., & Shearer, P. (2011). Imaging the lithosphere-asthenosphere boundary
963 beneath the Pacific using SS waveform modeling. *J. Geophys. Res.*, 116(7), B07307,
964 doi:07310.01029/02010JB008070.
- 965 Rychert, C. A., & Shearer, P. M. (2009). A Global View of the Lithosphere-Asthenosphere
966 Boundary. *Science*, 324(5926), 495-498. doi:Doi 10.1126/science.1169754
- 967 Rychert, C. A., Tharimena, S., Harmon, N., Wang, S., Constable, S., Kendall, J. M., . . .
968 Schlaphorst, D. (2021). A dynamic lithosphere-asthenosphere boundary near the
969 equatorial Mid-Atlantic Ridge. *Earth and Planetary Science Letters*, 566, 116949.
970 doi:<https://doi.org/10.1016/j.epsl.2021.116949>
- 971 Saikia, U., Rychert, C., Harmon, N., & Kendall, J. M. (2021). Upper Mantle Anisotropic Shear
972 Velocity Structure at the Equatorial Mid-Atlantic Ridge Constrained by Rayleigh
973 Wave Group Velocity Analysis From the PI-LAB Experiment. *Geochemistry,*
974 *Geophysics, Geosystems*, 22(3), e2020GC009495.
975 doi:<https://doi.org/10.1029/2020GC009495>
- 976 Schmeling, H. (1985). Numerical-Models on the Influence of Partial Melt on Elastic, Anelastic
977 and Electric Properties of Rocks .1. Elasticity and Anelasticity. *Phys. Earth Plan. Inter.*,
978 41(1), 34-57. doi:Doi 10.1016/0031-9201(85)90100-1
- 979 Schmerr, N. (2012). The Gutenberg Discontinuity: Melt at the Lithosphere-Asthenosphere
980 Boundary. *Science*, 335(6075), 1480-1483. doi:10.1126/science.1215433
- 981 Schutt, D. L., & Lesher, C. E. (2006). Effects of melt depletion on the density and seismic
982 velocity of garnet and spinel Iherzolite. *Journal of Geophysical Research-Solid Earth*,
983 111(B5), doi:10.1029/2003JB002950. doi:Artn B05401
984 Doi 10.1029/2003jb002950
- 985 Seton, M., Müller, R. D., Zahirovic, S., Williams, S., Wright, N. M., Cannon, J., . . . McGirr, R.
986 (2020). A Global Data Set of Present-Day Oceanic Crustal Age and Seafloor Spreading
987 Parameters. *Geochemistry, Geophysics, Geosystems*, 21(10), e2020GC009214.
988 doi:<https://doi.org/10.1029/2020GC009214>
- 989 Sifre, D., Gardes, E., Massuyeau, M., Hashim, L., Hier-Majumder, S., & Gaillard, F. (2014).
990 Electrical conductivity during incipient melting in the oceanic low-velocity zone.
991 *Nature*, 509(7498), 81-. doi:10.1038/nature13245
- 992 Sim, S. J., Spiegelman, M., Stegman, D. R., & Wilson, C. (2020). The influence of spreading
993 rate and permeability on melt focusing beneath mid-ocean ridges. *Phys. Earth Plan.*
994 *Inter.*, 304. doi:ARTN 106486
995 10.1016/j.pepi.2020.106486
- 996 Smith, W. H. F., & Sandwell, D. T. (1997). Global seafloor topography from satellite altimetry
997 and ship soundings. *Science*, 277, 1957-1962.
- 998 Spiegelman, M., & Elliott, T. (1993). Consequences of melt transport for uranium series
999 disequilibrium in young lavas. *Earth and Planetary Science Letters*, 118(1), 1-20.
1000 doi:[https://doi.org/10.1016/0012-821X\(93\)90155-3](https://doi.org/10.1016/0012-821X(93)90155-3)
- 1001 Stern, T. A., Henrys, S. A., Okaya, D., Louie, J. N., Savage, M. K., Lamb, S., . . . Iwasaki, T.
1002 (2015). A seismic reflection image for the base of a tectonic plate. *Nature*,
1003 518(7537), 85-. doi:10.1038/nature14146
- 1004 Stesky, R. M., & Brace, W. F. (1973). Electrical Conductivity of Serpentinized Rocks to 6
1005 Kilobars. *Journal of Geophysical Research*, 78(32), 7614-7621. doi:DOI
1006 10.1029/JB078i032p07614

- 1007 Stixrude, L., & Lithgow-Bertelloni, C. (2005). Mineralogy and elasticity of the oceanic upper
1008 mantle: Origin of the low-velocity zone. *J. Geophys. Res.*, 110, B03204,
1009 03210.01029/02004JB002965.
- 1010 Sun, J., & Li, Y. (2016). Joint inversion of multiple geophysical and petrophysical data using
1011 generalized fuzzy clustering algorithms. *Geophys. J. Int.*, 208(2), 1201-1216.
1012 doi:10.1093/gji/ggw442
- 1013 Takei, Y. (1998). Constitutive mechanical relations of solid-liquid composites in terms of
1014 grain-boundary contiguity. *Journal of Geophysical Research: Solid Earth*, 103(B8),
1015 18183-18203. doi:<https://doi.org/10.1029/98JB01489>
- 1016 Takougang, E. M. T., Harris, B., Kepic, A., & Le, C. V. A. (2015). Cooperative joint inversion of
1017 3D seismic and magnetotelluric data: With application in a mineral province.
1018 *Geophysics*, 80(4), R175-R187. doi:10.1190/geo2014-0252.1
- 1019 Tan, Y., & Helmberger, D. V. (2007). Trans-Pacific upper mantle shear velocity structure. *J.*
1020 *Geophys. Res.*, 112(8), B08301, doi:08310.01029/02006JB004853.
- 1021 Tharimena, S., Rychert, C., Harmon, N., & White, P. (2017). Imaging Pacific lithosphere
1022 seismic discontinuitiesInsights from SS precursor modeling. *Journal of Geophysical*
1023 *Research-Solid Earth*, 122(3), 2131-2152. doi:10.1002/2016jb013526
- 1024 Turcotte, D., & Schubert, G. (2002). *Geodynamics* (2nd ed.). Cambridge: Cambridge
1025 University Press.
- 1026 Wang, S., Constable, S., Reyes-Ortega, V., Jahandari, H., Farquharson, C., & Esquivel, T. A.
1027 (2021). Two-dimensional determinant inversion of marine magnetotelluric data and
1028 a field example from the Gulf of California, Mexico. *Geophysics*, 86(1), E37-E57.
1029 doi:10.1190/geo2019-0735.1
- 1030 Wang, S. G., Constable, S., Reyes-Ortega, V., & Rychert, C. A. (2019). A newly distinguished
1031 marine magnetotelluric coast effect sensitive to the lithosphere-asthenosphere
1032 boundary. *Geophys. J. Int.*, 218(2), 978-987. doi:10.1093/gji/ggz202
- 1033 Wang, S. G., Constable, S., Rychert, C. A., & Harmon, N. (2020). A Lithosphere-
1034 Asthenosphere Boundary and Partial Melt Estimated Using Marine Magnetotelluric
1035 Data at the Central Middle Atlantic Ridge. *Geochemistry Geophysics Geosystems*,
1036 21(9). doi:ARTN e2020GC009177
1037 10.1029/2020GC009177
- 1038 Workman, R. K., & Hart, S. R. (2005). Major and trace element composition of the depleted
1039 MORB mantle (DMM). *Earth and Planetary Science Letters*, 231(1-2), 53-72.
1040 doi:10.1016/j.epsl.2004.12.005
- 1041 Yamauchi, H., & Takei, Y. (2016). Polycrystal anelasticity at near-solidus temperatures.
1042 *Journal of Geophysical Research*, 121(11), 7790-7820. doi:10.1002/2016jb013316
- 1043 Zhang, R., Li, T., Deng, X., Huang, X., & Pak, Y. (2020). Two-dimensional data-space joint
1044 inversion of magnetotelluric, gravity, magnetic and seismic data with cross-gradient
1045 constraints. *Geophysical Prospecting*, 68(2), 721-731.
1046 doi:<https://doi.org/10.1111/1365-2478.12858>
- 1047

Figure 1.

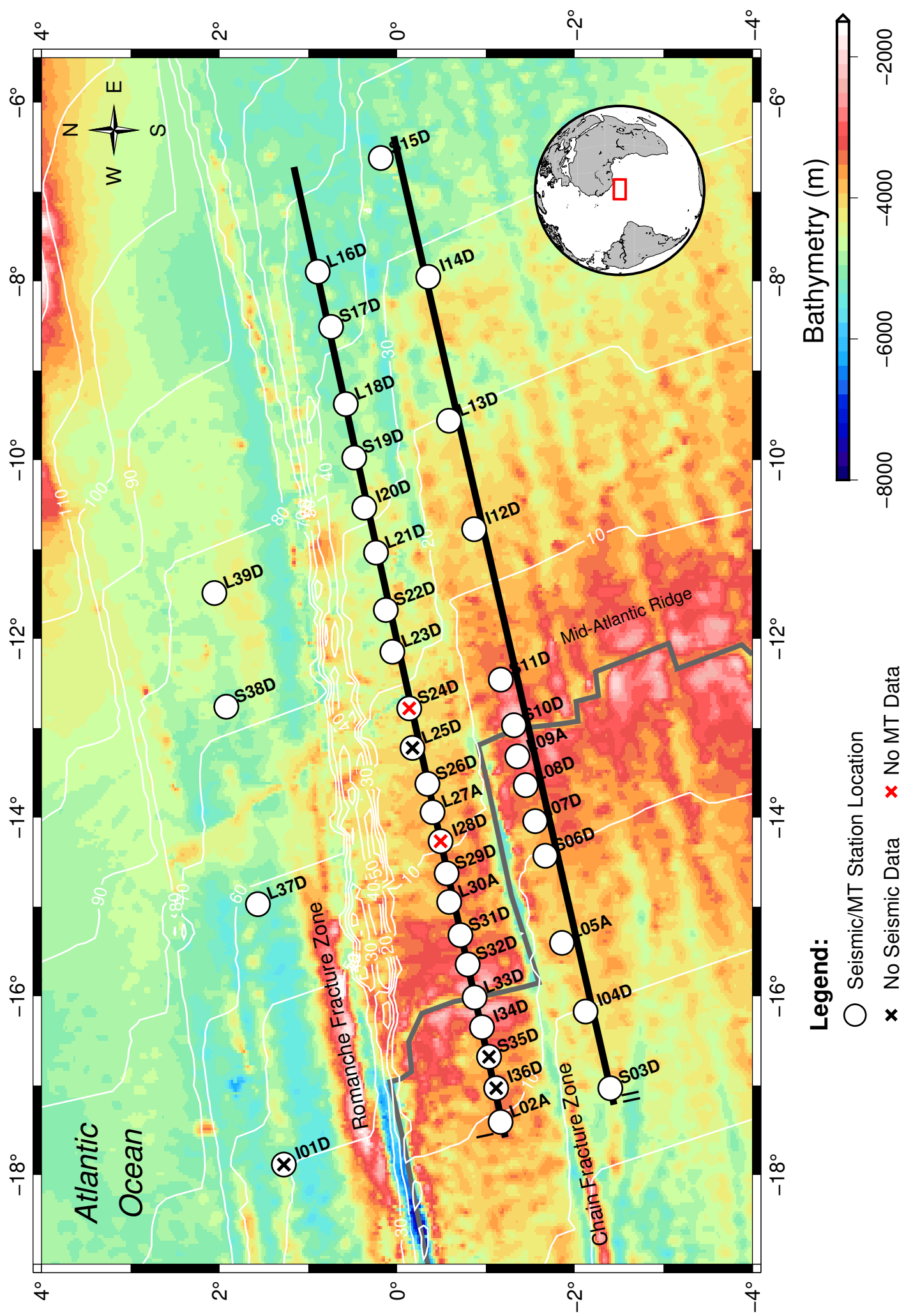


Figure 2.

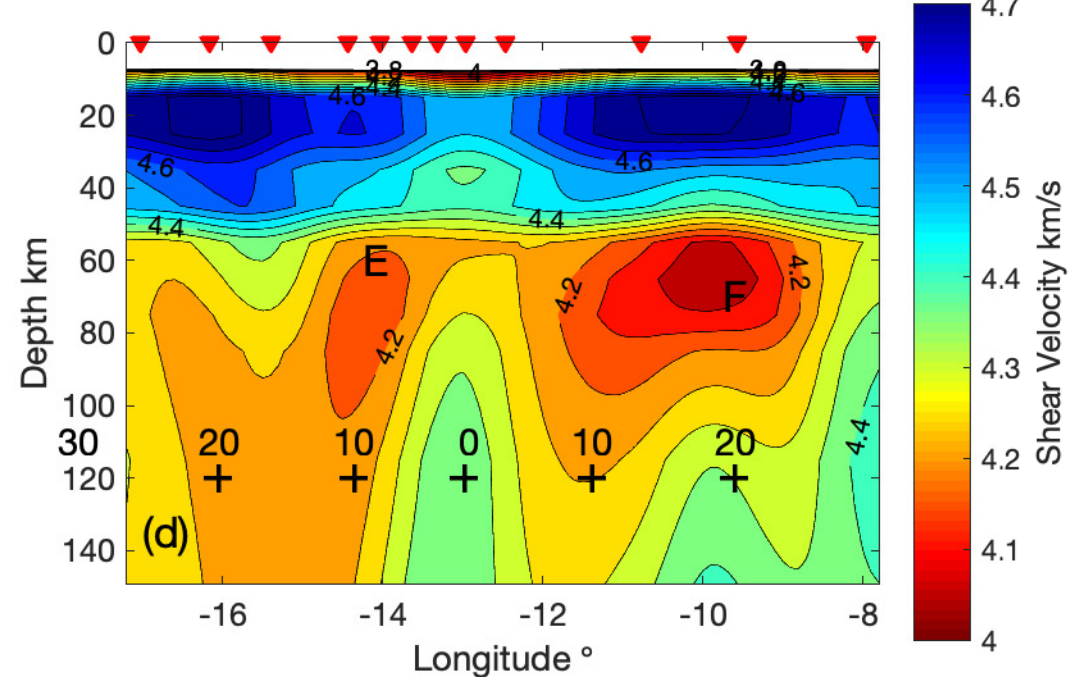
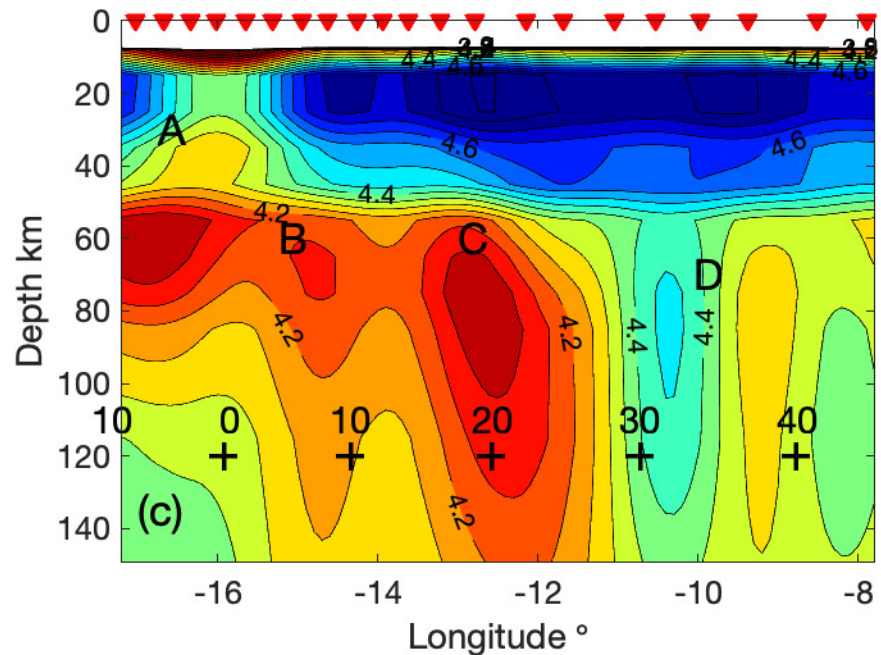
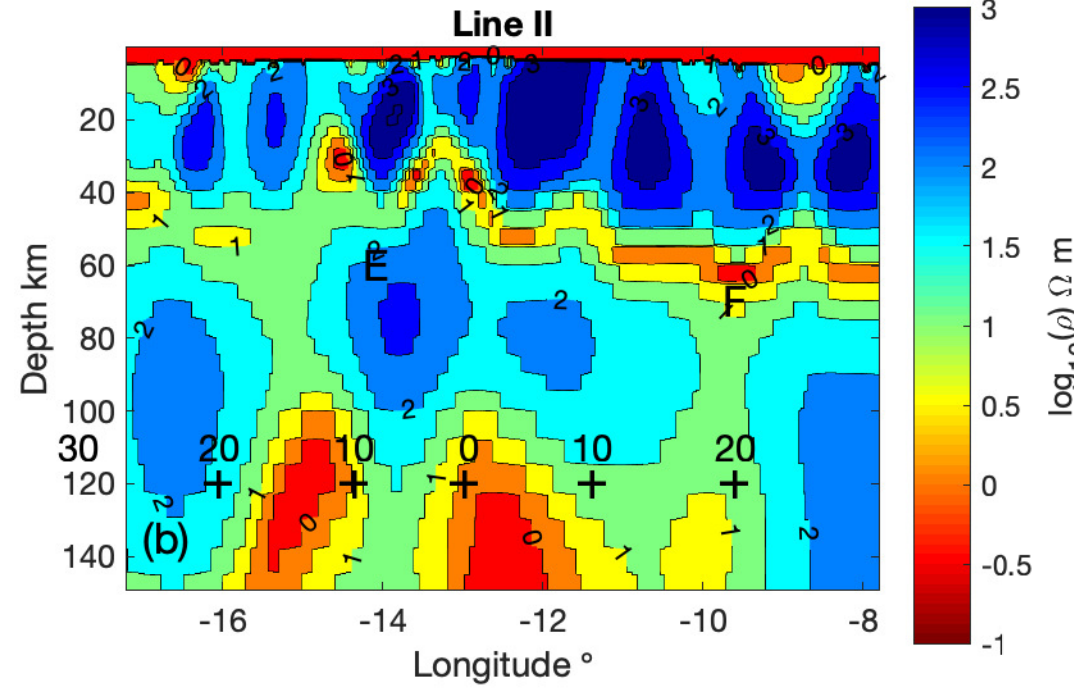
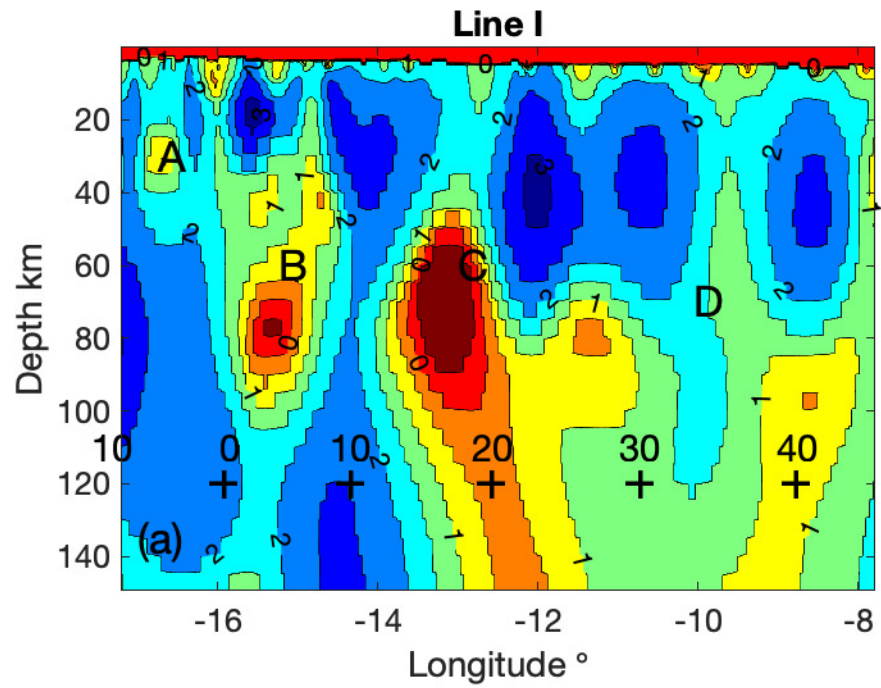


Figure 3.

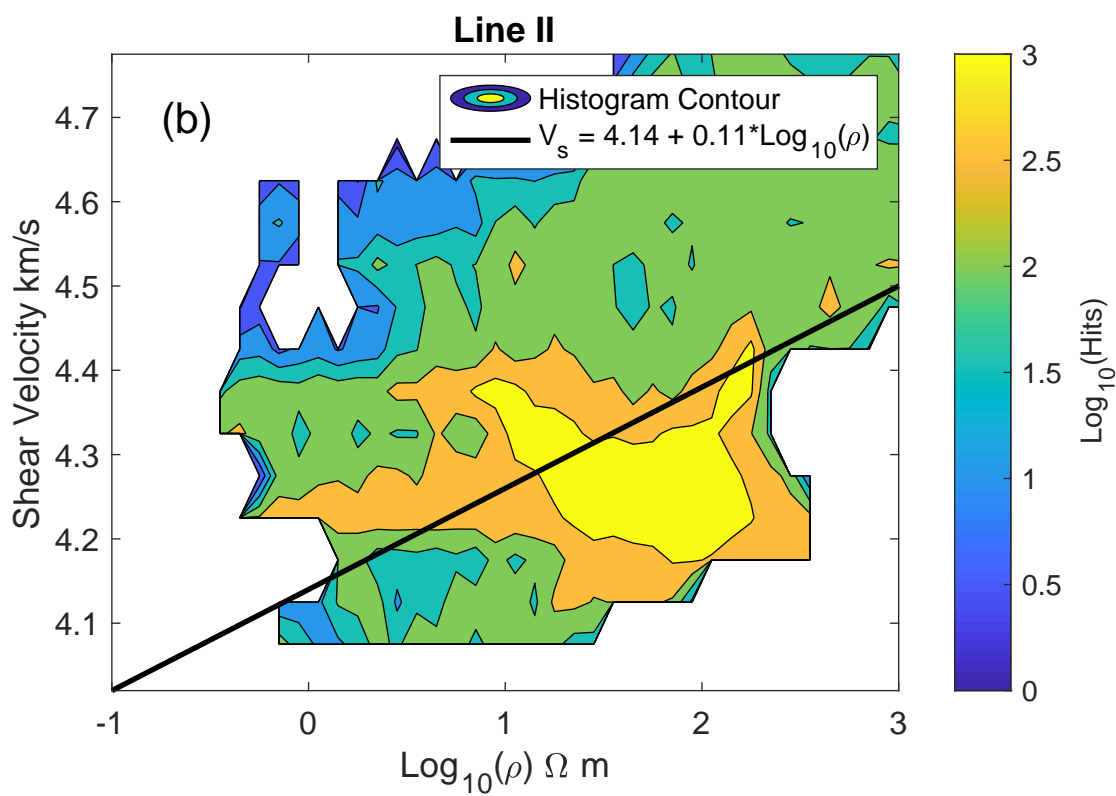
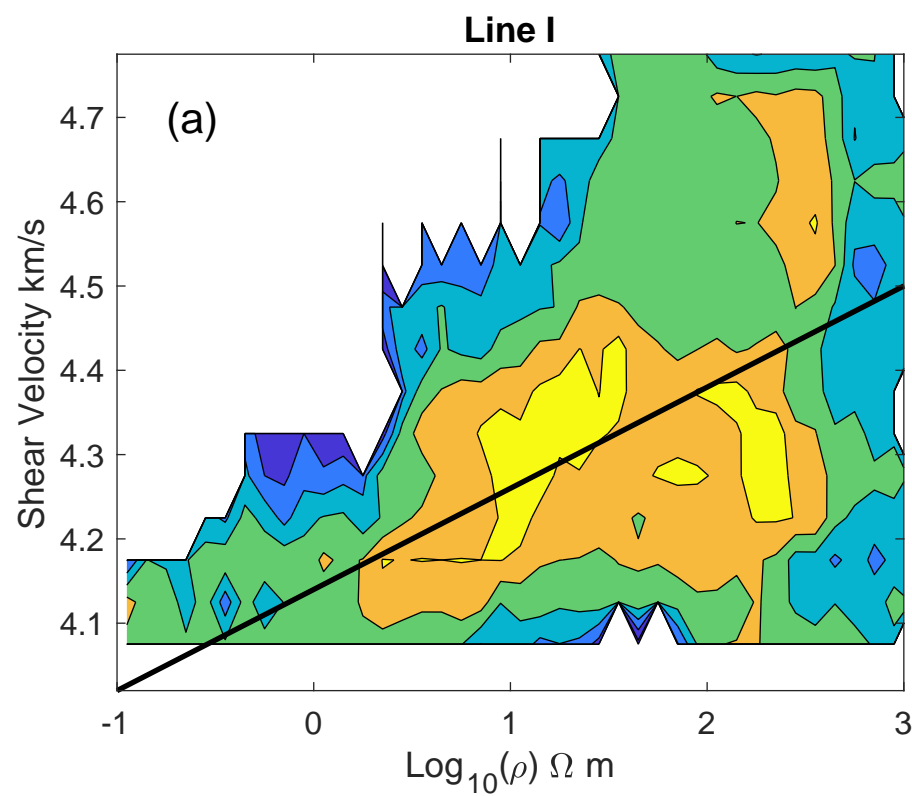


Figure 4.

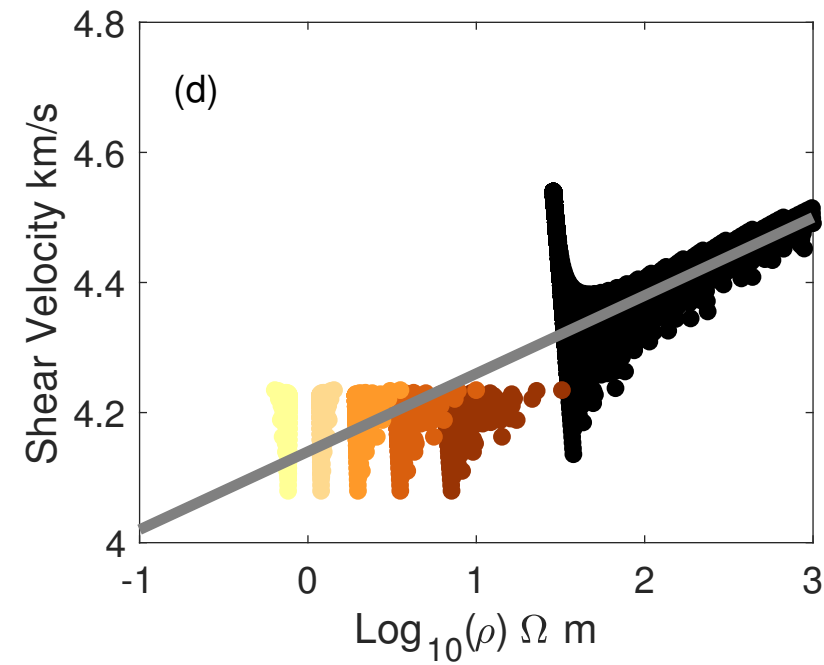
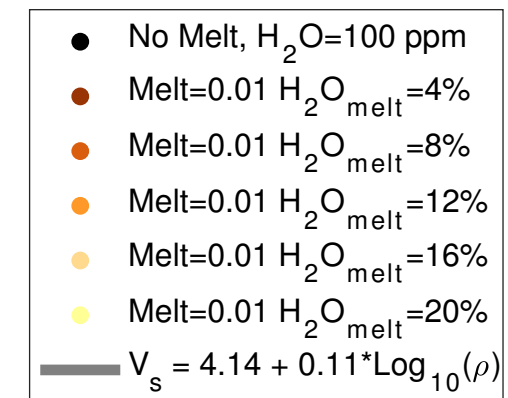
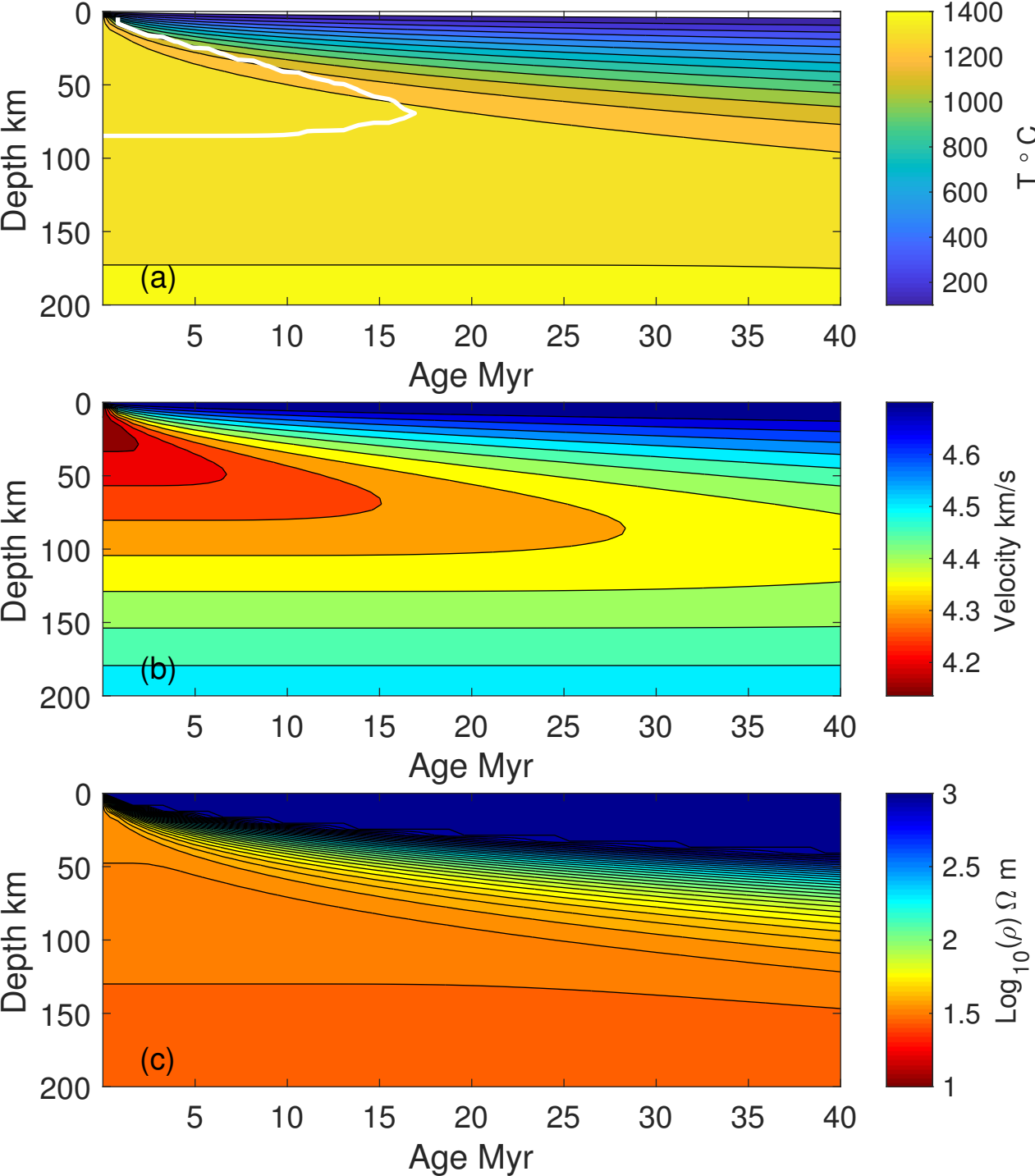


Figure 5.

— MT Start Final
 — 1D Start Final
 — MT Start Ini.
 — 1D Start Ini.

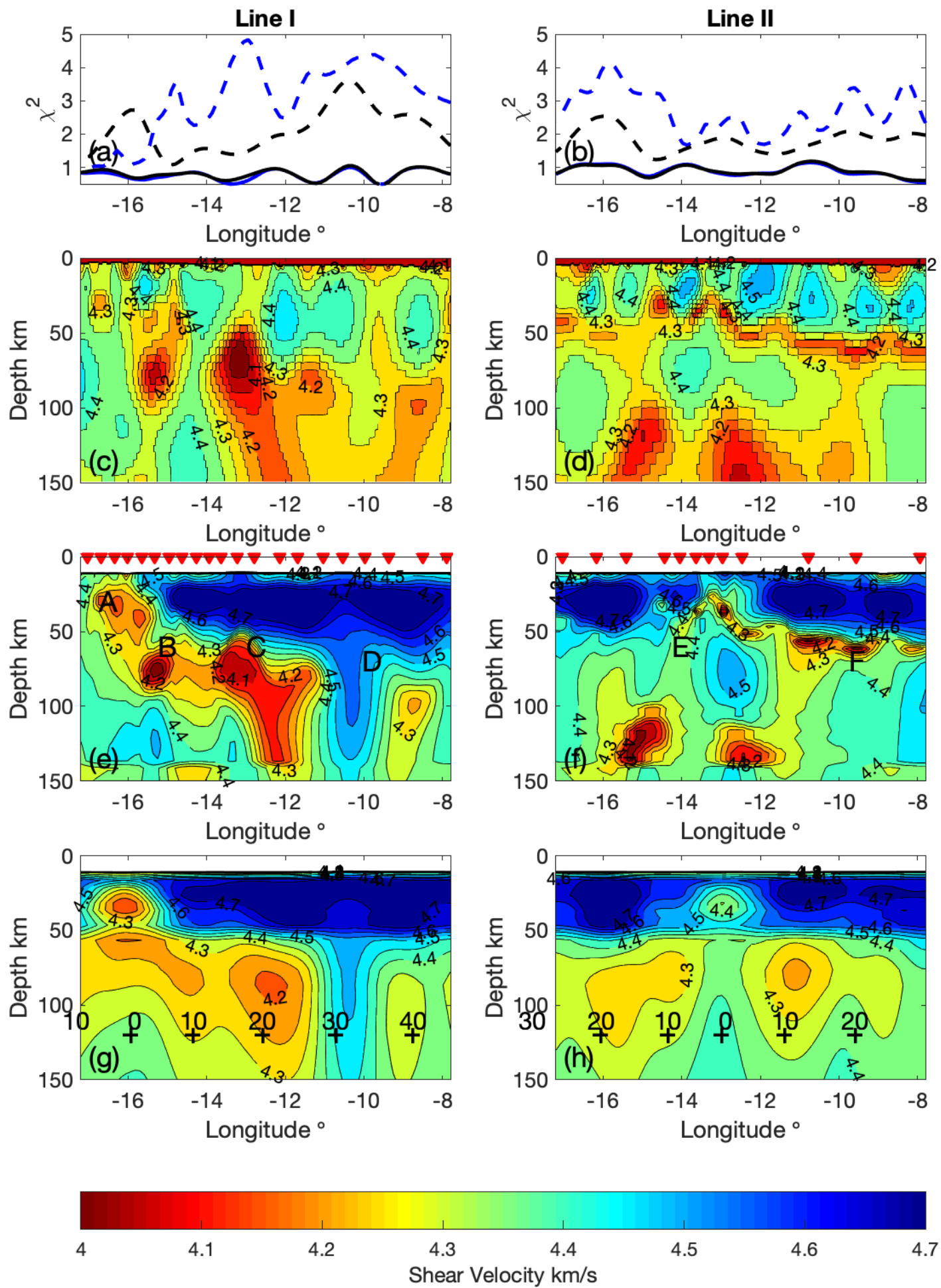


Figure 6.

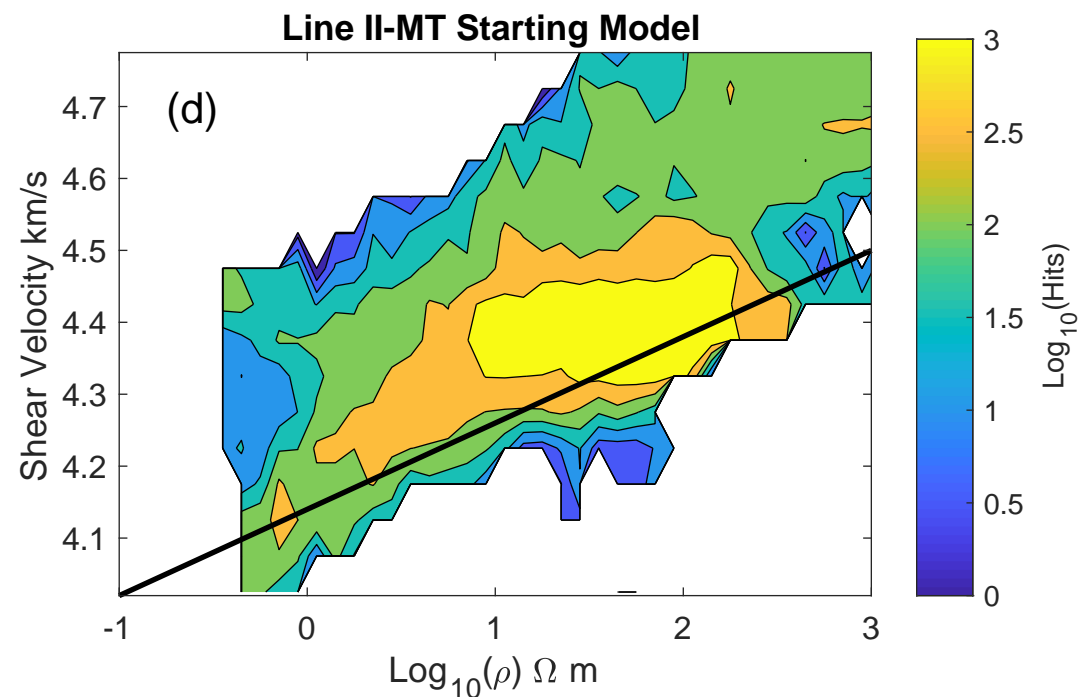
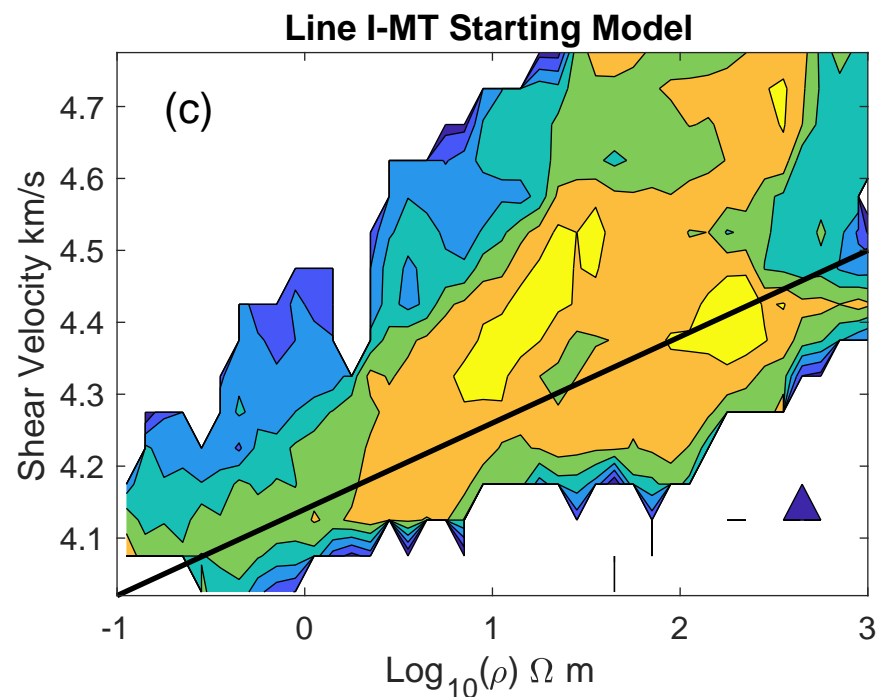
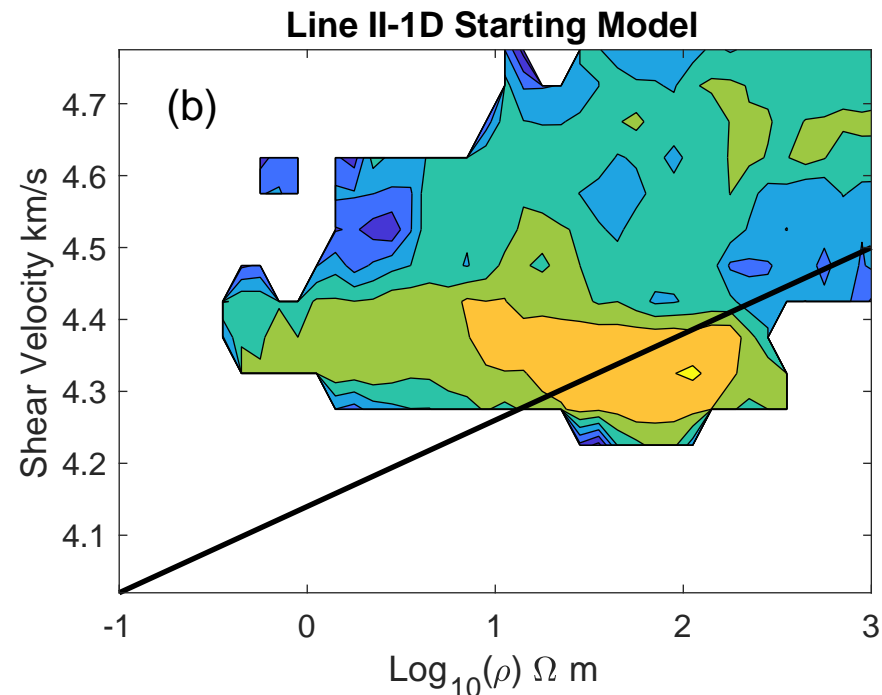
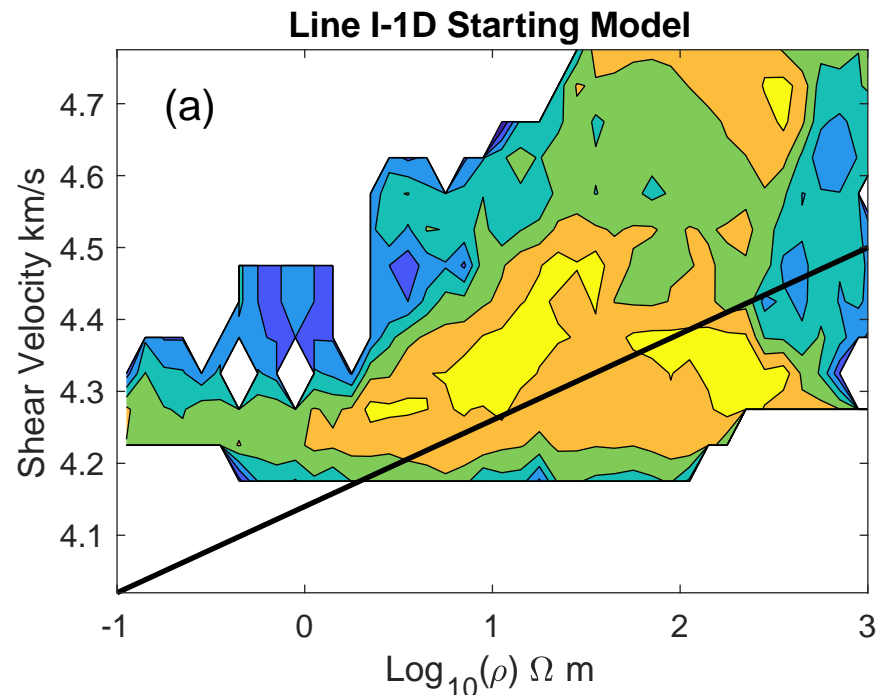


Figure 7.

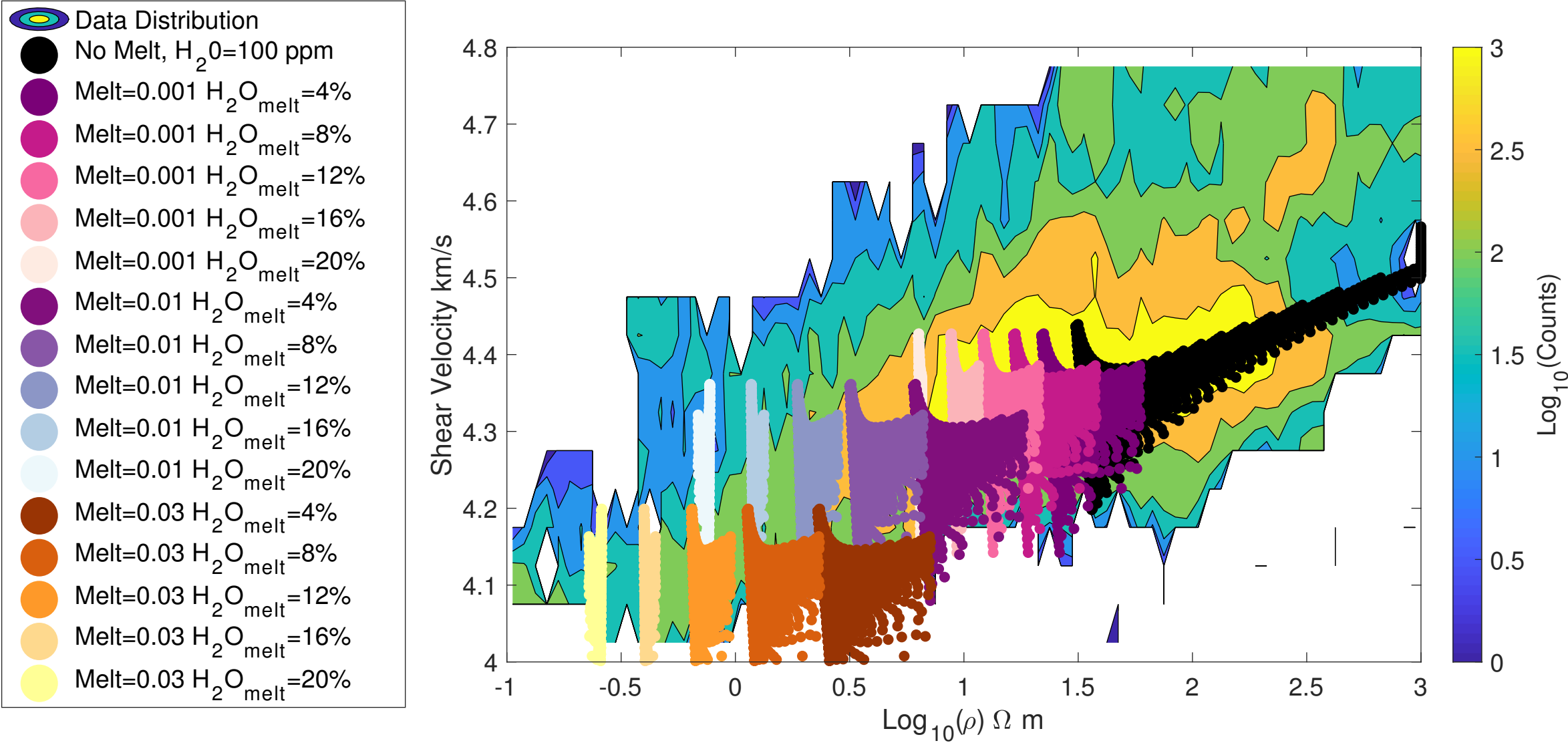


Figure 8.

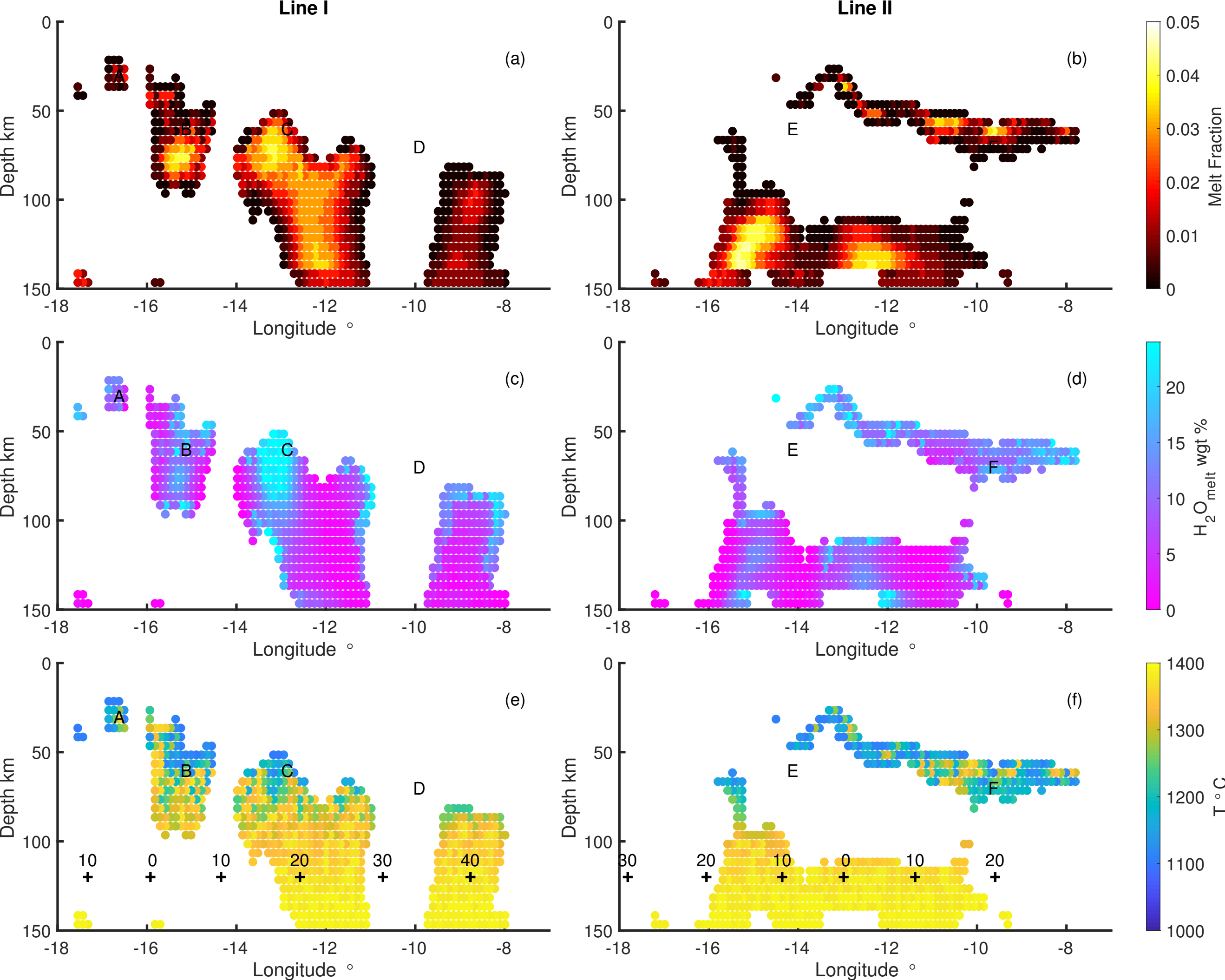


Figure 9.

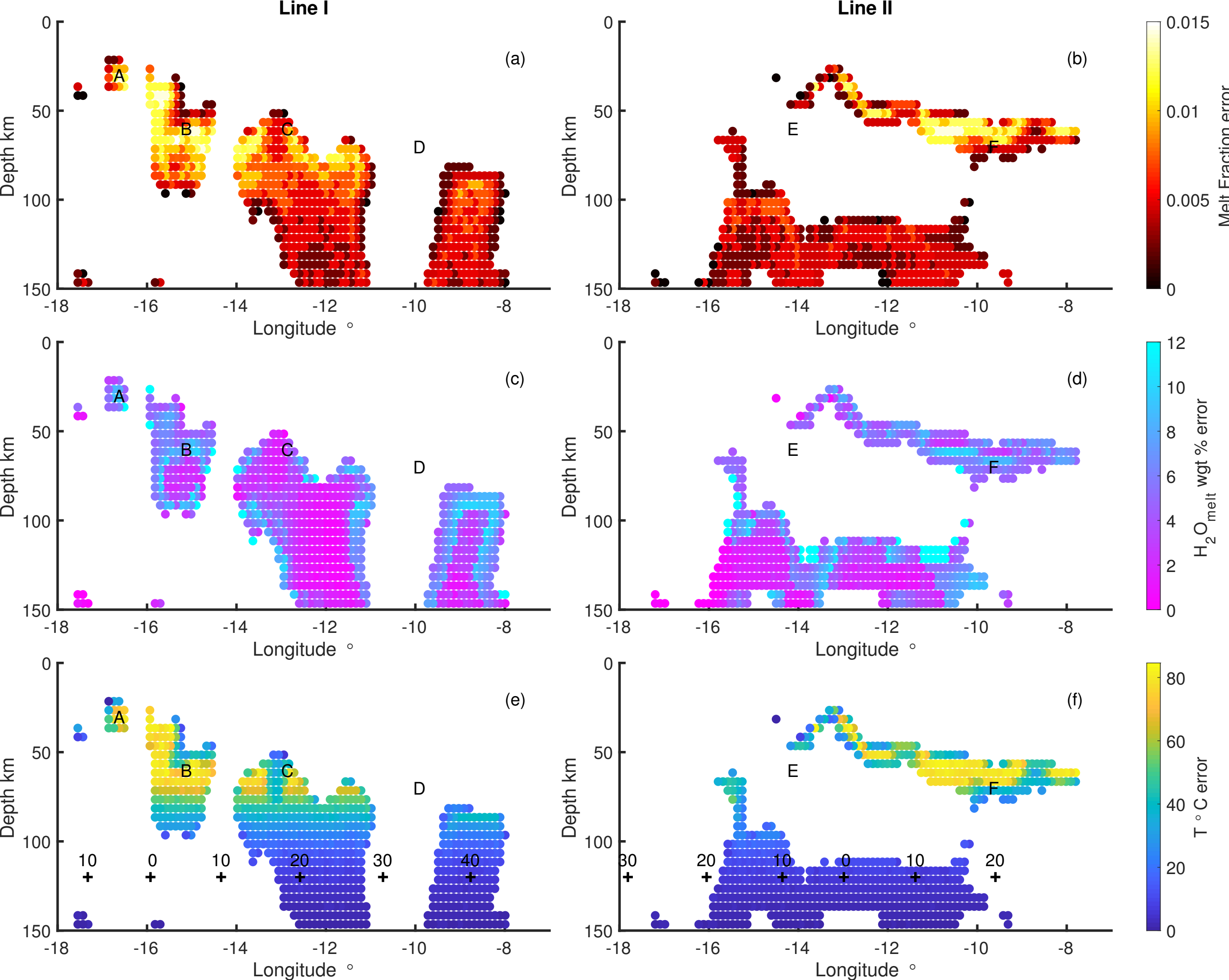


Figure 10.

